QUANTITATIVE SUSCEPTIBILITY MAPPING OF ATHEROSCLEROSIS IN CAROTID ARTERIES

QUANTITATIVE SUSCEPTIBILITY MAPPING OF ATHEROSCLEROSIS IN CAROTID ARTERIES

BY

CHAOYUE WANG B.Sc.

A Thesis

Submitted to the School of Graduate Studies

in Partial Fulfillment of the Requirements

for the Degree of

M.A.Sc.

(Master of Applied Science)

in Biomedical Engineering

McMaster University

M. A. Sc. (2017) McMaster University

(School of Biomedical Engineering) Hamilton, Ontario, Canada

TITLE: Quantitative Susceptibility Mapping of Atherosclerosis in Carotid Arteries

AUTHOR: Chaoyue Wang
B.Sc., (Biomedical Engineering)
Zhejiang University
Hangzhou, China

SUPERVISOR: E. Mark. Haacke, Ph.D.

NUMBER OF PAGES: xii, 82

Abstract

Carotid atherosclerosis, one of the leading causes of ischemic stroke worldwide, can induce severe narrowing or even occlusion of the vessel, restricting blood flow to the brain and resulting in perfusion deficits. The plaque that has a high probability of undergoing rapid progression or future ruptures is defined as “vulnerable plaque”. Identifying vulnerable plaque is of great importance in clinical carotid atherosclerosis imaging. To date, a multi-contrast magnitude-based MR approach with blood suppression technique has been widely used to detect vulnerable plaque features. However, due to the limitations of magnitude-based methods, developing new MR techniques that have better sensitivity to hemorrhage and calcification is of great interest.

Quantitative Susceptibility Mapping (QSM) is a technique that utilizes the MR phase information and has been widely used for quantifying the tissue susceptibility in the brain. The susceptibility contrast is extremely sensitive to hemorrhage and calcium which makes QSM a potential tool for carotid plaque imaging to identify intraplaque hemorrhage (IPH) and calcification. However, existing QSM methods have not been successfully implemented in the neck due to several challenges. The presence of air/tissue interface, plaque that has high susceptibility, and fat surrounding the carotid arteries can cause severe phase aliasing and other problems that will induce errors in the resultant susceptibility maps. To overcome these challenges and thus, develop a robust method for carotid QSM, a protocol that includes both data acquisition strategy and post-processing methods is

proposed. For data acquisition, four echoes including two water/fat in-phase echoes and two water/fat out-of-phase echoes were collected. For data post-processing, temporal domain algorithm Catalytic Multiecho Phase Unwrapping Scheme (CAMPUS) was used to unwrap the phase images and local QSM was proposed. This protocol is able to properly unwrap the phase images even with the presence of high susceptibility plaque and eliminate the water/fat chemical shift effect in QSM reconstructions which will generate reliable susceptibility maps. From our results, the proposed QSM protocol has demonstrated the ability to generate reliable susceptibility maps and excellent sensitivity to IPH and calcification. Combining QSM with existing magnitude-based methods will lead to a major improvement in the diagnosis of carotid atherosclerosis.

Acknowledgements

I would like to express my deepest appreciation to my supervisor, Dr. E. Mark Haacke, for his enduring guidance and support throughout my study at McMaster University. Even with his busy schedule, Dr. Haacke always has time to teach me and answer my questions. As one of the leading scientists in MRI field, Dr. Haacke and his passion for research have been and will always be an inspiration to me. It has been a great honour for me to work under his guidance.

I would like to sincerely thank Dr. Michael Noseworthy for all his guidance and help during my time at McMaster University. His lectures have been both informative and exciting. Thanks to my supervisory committee member, Dr. Qiyin Fang, for his valuable guidance and comments.

I would like to thank Dr. Saifeng Liu, Dr. Sagar Buch for their enormous help and the time they spent in reviewing my thesis. Thanks to Dr. Jaladhar Neelavalli for all his guidance and help. It has been a great privilege to work with them.

Finally, I wish to thank my parents, my mother, Suping Wang and my father, Qi Wang, for the endless love and support they gave me throughout my life. This thesis is dedicated to my parents.

Contents

List of Figures

Chapter 2

Chapter 3

Chapter 4

List of Tables

Chapter 3

Chapter 4

List of Abbreviations

3DSRNCP	Quality guided 3D phase unwrapping algorithm
AHA	American Heart Association
BW	Bandwidth
CAS	Carotid artery stenting
CAMPUS	Catalytic multiecho phase unwrapping scheme
CE	Contrast enhanced
CEA	Carotid endarterectomy
COSMOS	Calculation of susceptibility through multiple orientation sampling
CSF	Cerebrospinal fluid
FA	Flip angle
FC	Fibrous cap
FOV	Field of view
GRE	Gradient echo
Hct	Hematocrit
IPH	Intraplaque hemorrhage
LRNC	Lipid-rich necrotic core
MERGE	Motion-sensitized driven equilibrium prepared rapid gradient echo
MIP	Maximum intensity projection
MPRAGE	magnetization prepared rapid acquisition gradient echo
MRI	Magnetic resonance imaging
MSPREP	Motion-sensitizing magnetization preparation

PD	Proton density
PDF	Projection onto the dipole field
QSM	Quantitative susceptibility mapping
RF	Radio-frequency
ROI	Region of interest
SHARP	Sophisticated harmonic artifact reduction for phase data
SNR	Signal-to-noise ratio
SSFP	Steady-state free-precession
SWI	Susceptibility weighted imaging
TE	Echo Time
th	Threshold
TOF	Time of flight
TR	Repetition time
TES	Turbo spin echo

Chapter 1 Introduction

Magnetic resonance imaging (MRI) is a non-invasive imaging modality that provides both structural and functional information of different tissues with magnitude and phase images. Magnitude images have been primarily used in clinical MRI applications due to its excellent soft tissue contrast. By altering the sequence design and associated imaging parameters, a variety of contrasts can be generated between different tissues [1].

Since the beginning of MRI, phase images have been used for a few applications such as chemical shift imaging, flow quantification and MRI thermometry. However, in clinical settings, most phase images have been ignored until susceptibility weighted imaging (SWI) was invented. In SWI, phase images are used to generate filtered phase images that combining with magnitude images enhances a susceptibility-weighted contrast. This enhanced contrast is sensitive to the iron and calcium substances (e.g., veins and microbleeds in the brain) [2]. Although the potential of SWI technique has already been demonstrated in many clinical applications, it is limited by the orientation dependence of phase information [2]. It is rather difficult to quantitatively measure the iron or calcium content using SWI [3]. Thus, obtaining the source image (susceptibility map) that has no orientation or imaging parameter dependence is of great importance.

Magnetic susceptibility is a fundamental property of all materials [3]. Quantitative Susceptibility Mapping (QSM), a realtively new MR technique, can provide a robust means to depict and quantify tissue magnetic susceptibility sources, which includes paramagnetic substance (e.g., iron content) and diamagnetic substance (e.g., myelin content) in brain tissues [4]. Note that, the susceptibility of blood varies as a function of the blood oxygenation level which is discussed in Chapter 2 [4]. Thus, QSM has been widely used as a tool for quantifying the tissue susceptibility in the brain, such as the quantification of iron deposition and venous oxygen saturation as well as for stroke diagnosis [4, 5].

Stroke has become one of the leading causes of death and disability worldwide [6]. Carotid artery atherosclerosis, one of the major causes of ischemic stroke, can induce severe narrowing or even occlusion of the vessel, restricting blood flow to the brain and resulting in perfusion deficits [6]. So, the primary goal of carotid atherosclerosis imaging is to identify lesions that will lead to ischemic stroke. The presence of carotid plaques can be categorized into two types, 1) a stable plaque that progresses over time and restricts blood flow *in situ*; and 2) an unstable plaque that is likely to rupture and cause ischemic stroke in the future. The plaque with a high probability of undergoing rapid progression or future rupture is defined as vulnerable plaque [7]. Histological studies have led to the conclusions that plaques with large lipid-rich necrotic cores, thin fibrous cap rupture, intraplaque hemorrhage, plaque neovasculature and vessel wall inflammation are characterized as vulnerable plaques [8]. Thus, being able to characterize the type of plaque will have an

immediate impact on not only the diagnosis of carotid artery atherosclerosis but also on the choice of treatment for the patient.

A variety of MRI methods has been used for carotid atherosclerosis imaging over the years including different contrast weighting information. Most of the existing techniques are based on blood flow suppression method such as black or bright blood technique with different contrast mechanism, including T1, T2, and other contrast weightings [9]. These methods have been demonstrated the ability to distinguish between different types of atherosclerotic plaque by analyzing their signal intensities and morphological appearances [9]. Although well accepted, these techniques have a few shortcomings: The first is the fundamental limitation of magnitude information, because it is indirect information, in order to differentiate different types of plaque, magnitude images with at least three contrast weightings are needed which will increase the scan time. The second is the potential incomplete suppression of flow (especially complex flow at the carotid artery bifurcation) which can lead to artifacts, thus misinterpretation of vessel wall that can lead to an overestimation of the wall thickness. The third disadvantage is that both 2D and 3D methods need long scan times and, hence, are sensitive to motion [10]. A more detailed overview of the carotid vessel wall and plaque imaging is introduced in Chapter 3.

Susceptibility maps are generated from phase data collected using SWI sequence. SWI sequence is a fully flow-compensated GRE sequence that has full region of interest (ROI) coverage in 3D without the need to suppress the blood signal [3]. The susceptibility

difference between arterial blood, vessel wall and different plaque types (fibrosis, hemorrhage, calcium) makes QSM a potential tool for characterizing atherosclerotic plaque [4].

However, existing QSM techniques have not been successfully implemented in the neck due to several challenges including, (1) the presence of air/tissue interface (trachea) close to carotid arteries that will cause sever phase aliasing; (2) the potential presence of plaque with high susceptibility that will cause phase aliasing inaisde the plaque region; as well as (3) the presence of fat surrounding the carotid arteries and jugular veins. These challenges will be further elaborated in Chapter 4.

In order to overcome the above challenges, a neck QSM protocol is proposed. The proposed protocol for QSM of carotid atherosclerosis imaging includes both data acquisition strategy and post-processing methods. For data acquisition, collecting four echoes using 3D SWI sequence are proposed. The four echoes include two water/fat in-phase echoes and two water/fat out-of-phase echoes. For data post-processing, temporal domain algorithm Catalytic Multiecho Phase Unwrapping Scheme (CAMPUS) [11] is proposed to unwrap the original phase images and local QSM concept is proposed for QSM reconstruction. Combining two parts together enables the visualization of iron, calcium inside the plaque as well as water/fat saperation in the neck. This protocol will be further elaborated in Chapter 4.

References

1. Haacke et al, Magnetic Resonance Imaging: Physical Principles and Sequence Design, 1st Ed., Wiley- Liss;1999.

2. Haacke EM, Xu Y, Cheng YCN, Reichenbach JR. Susceptibility weighted imaging (SWI). Magn. Reson. Med. 2004;52:612-8.

3. Haacke EM, Mittal S, Wu Z, Neelavalli J, Cheng YCN. Susceptibility-Weighted Imaging: Technical Aspects and Clinical Applications, Part 1. Am. J. Neuroradiol. 2009;30:19-30.

4. Haacke, E. Mark, et al. Quantitative susceptibility mapping: current status and future directions. Magnetic resonance imaging 33.1 (2015): 1-25.

5. Haacke EM, Tang J, Neelavalli J, Cheng YC. Susceptibility mapping as a means to visualize veins and quantify oxygen saturation. J. Magn. Reson. Imaging 2010; 32:663-76.

6. Kerwin, William S. Carotid artery disease and stroke: assessing risk with vessel wall MRI. ISRN cardiology 2012 (2012).

7. Underhill, Hunter R., et al. MRI of carotid atherosclerosis: clinical implications and future directions. Nature Reviews Cardiology 7.3 (2010): 165-173.

8. Cai, Jian-Ming, et al. Classification of human carotid atherosclerotic lesions with in vivo multicontrast magnetic resonance imaging. Circulation 106.11 (2002): 1368-1373.

9. Yuan, Chun, et al. MRI of carotid atherosclerosis. Journal of nuclear cardiology 15.2 (2008): 266-275.

10. Yuan, Chun, and Dennis L. Parker. Three-Dimensional Carotid Plaque MR Imaging. Neuroimaging Clinics of North America 26.1 (2016): 1-12.

11. Feng W, Neelavalli J, Haacke EM. Catalytic multiecho phase unwrapping scheme (CAMPUS) in multiecho gradient echo imaging: removing phase wraps on a voxel-by-voxel basis. Magn Reson Med 2013;70(1):117–26.

Chapter 2 Basic Concepts of MR Phase Signal, Gradient Echo, and Quantitative Susceptibility Mapping[1]

2.1 The formation of MR signal

In the presence of an external magnetic field $\vec{B}_0$, the interaction of spins with the magnetic field can be understand as the spins precessing around the field direction. The recession frequency is given by:

$$\omega_0 = \gamma B_0 \qquad [2.1]$$

where ω_0 is referred to as the Larmor frequency, γ is the gyromagnetic ratio (for a hydrogen proton $\gamma = 2.68\times10^8\ rad/s/Tesla$). The net magnetization of the spins is in the direction of the magnetic field. After the application of a radio-frequency (RF) pulse, the magnetization of the spins is rotated along the applied RF pulse (away from the main magnetic field), thus, generates two magnetization components in the transverse and longitude directions. Due to the short temporary presence of this RF pulse, the

[1]Most of the contents in this chapter are adapted from Haacke EM, et al. Magnetic Resonance Imaging: Physical Principles and Sequence Design. 1st ed. Wiley-Liss; 1999, and Haacke EM, Reichenbach JR, editors. Susceptibility Weighted Imaging in MRI: Basic Concepts and Clinical Applications. 1st ed. Wiley-Blackwell; 2011.

magnetization of the spins will then rotate back to the direction of the main field, thus, the longitudinal magnetization will experience regrowth and the transverse magnetization will decay. This process is described by the Bloch Equations [1]. The regrowth rate of the longitudinal magnetization is defined by the spin-lattice relaxation time, represented by T_1. The decaying rate of the magnetization in the transverse plane is defined by spin-spin relaxation time, represented by T_2. In practice, there is an additional dephasing of the transverse magnetization introduced by external field inhomogeneities, which can be characterized by a separate decay time T_2' thus, the total relaxation decay rate is described using the T_2^* time constant, which is defined as:

$$\frac{1}{T_2^*} = \frac{1}{T_2} + \frac{1}{T_2'} \quad [2.2]$$

In MRI, apart from the RF excitation pulse, additional external gradients coils are also needed in order to produce spatially dependent signal from given tissues. When applying three gradients $G_x(t)$, $G_y(t)$ and $G_z(t)$ in x-y-z directions, the subject experiences a time-varying magnetic field, which is given by:

$$B(\vec{x}, \vec{y}, \vec{z}, t) = \overrightarrow{B_0} + G_x(t) \cdot \vec{x} + G_y(t) \cdot \vec{y} + G_z(t) \cdot \vec{z} \quad [2.3]$$

Define $\rho(x, y, z)$ as the effective proton density and

$$k_x(t) = \gamma \int_0^t dt' G_x(t'),\ k_y(t) = \gamma \int_0^t dt' G_y(t'),\ k_z(t) = \gamma \int_0^t dt' G_z(t') \quad [2.4]$$

where $\gamma = \gamma/2\pi$. The signal expression can be written as:

$$s(k_x, k_y, k_z) = \iiint dx dy dz\ \rho(\vec{x}, \vec{y}, \vec{z})\, e^{-2\pi i(k_x\vec{x} + k_y\vec{y} + k_z\vec{z}, t)} \quad [2.5]$$

Eq. 2.5 indicates that the signal is the Fourier transform of the effective proton density, $\rho(\vec{x},\vec{y},\vec{z})$. In MRI, the data ($k$) space defined by Eq. 2.5 is called "k-space". MR magnitude and phase images can then be generated from the complex data of $\rho(\vec{x},\vec{y},\vec{z})$.

2.2 The concept of gradient echo (GRE)

The integration in Eq. 2.5 requires sufficient coverage of k-space to reconstruct the effective proton density. This can be achieved by varying the external gradients $G_x(t)$, $G_y(t)$ and $G_z(t)$. Define $G_S(t)$, $G_P(t)$ and $G_R(t)$ as the slice selection, phase encoding, and readout gradients, respectively. [2]. Gradient echo (GRE) imaging is one of the most important sequences being used in MRI experiments. A typical 3D GRE sequence diagram is shown in **Fig. 2.1**.

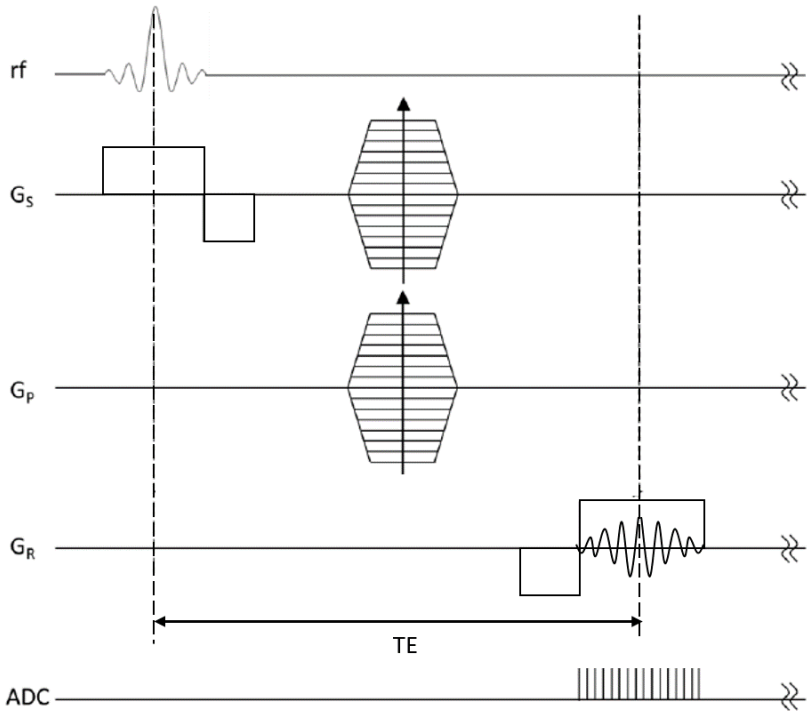

Figure 2.1 Sequence diagram of a single echo 3D gradient echo sequence. G_S: slice selection/partition encoding gradient; G_P: phase encoding gradient; G_R: readout gradient.

Note that, the sequence shown in **Fig. 2.1** is a simplified gradient echo sequence. The rapid and pulsatile flow of blood can cause signal variations that lead to artifacts in the image, such as signal loss due to flow-induced dephasing, misregistration artifacts and the velocity induced phase. The phase for a spin moving with constant velocity v along the read direction for a bipolar pulse G_x of duration 2τ is given by:

$$\phi = \lambda \cdot G_x \cdot v \cdot \tau^2 \qquad [2.6]$$

Flow compensation is a technique that modifies the gradient waveform in order to suppress the velocity induced phase [1, 2]. To achieve flow compensation, gradient moments nulling

technique is used. Gradient moments are calculated from the integral of a given gradient waveform with time which can be written as:

$$m_n = \int [t^n \cdot G(t)]\, dt \qquad [2.7]$$

where m_n is the nth gradient moment of the gradient waveform $G(t)$. Depending on the application, gradient moments of a gradient waveform can be nulled to different orders. Motion or flow with constant velocity is compensated by nulling the first moment of a gradient waveform [1].

Since the accuracy of SWI and QSM relies on extracting the phase information induced by susceptibility, for SWI and QSM data acquisition, flow compensation in slice selection, phase encoding and readout directions are usually required, in order to reduce the flow induced phase [2]. The sequence diagram of a 3D gradient echo sequence with full flow compensation is shown in **Fig. 2.3**. In case of series acquisitions, the remnant transverse magnetization after one acquisition (before the next RF pulse) should be destructed by applying spoiling gradients so that the transverse magnetization is purposefully made zero, this method generates a steady-state signal. The steady-state signal for a voxel for the spoiled gradient echo sequence is given by [1, 2]:

$$\hat{\rho}(\theta, TE) = \rho_0 sin\theta \frac{1-E_1}{1-E_1 cos\theta} e^{-TE/T_2^*} \qquad [2.8]$$

where ρ_0 is the voxel spin density, θ is the flip angle, and $E_1 = e^{-TR/T_1}$.

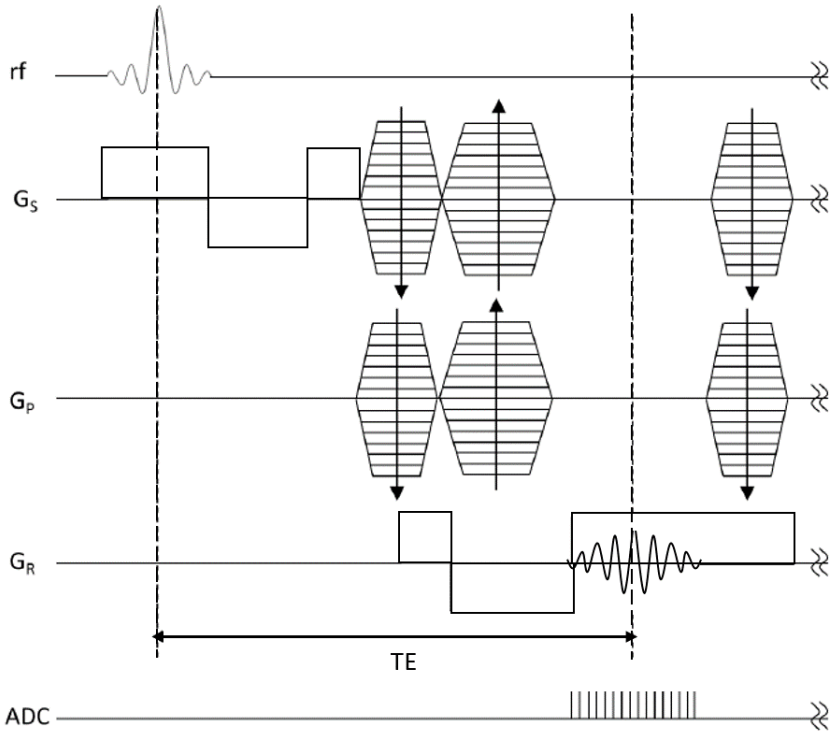

Figure 2.2 Sequence diagram of a single echo 3D gradient echo sequence with flow-compensation in all directions. G_S: slice selection/partition encoding gradient; G_P: phase encoding gradient; G_R: readout gradient.

Note that, the sequences shown in **Figs. 2.1** and **2.2** are single echo gradient echo sequences. A multi-echo gradient echo sequence can also be achieved by repeating the same gradients setting in one RF excitation period. This multi-echo approach enables acquiring MR data at different echo times during one excitation, which is important for SWI and QSM acquisitions [2].

2.3 Complex representation of MR signal and phase

Generally, phase can be defined as the changing orintation of the magetization vector in the transverse plane [2]. Thus, phase can be written as:

$$\phi(t) = \omega \cdot t \quad [2.9]$$

Assuming x-y represents the the transverse plane, the transverse magnetation vector $M_{xy}(\vec{r}, t)$ at position $\vec{r}$ can be represented by:

$$M_{xy}(\vec{r}, t) = M_{xy}(\vec{r}, t) \cdot e^{i\phi(\vec{r},t)} \quad [2.10]$$

Thus, any vector $\rho = (x, y)$ in the trasverse plane can be written as:

$$\rho = \rho_x + \rho_y$$

or, in complex notation, $$\rho = |\rho| \cdot e^{i\phi} \quad [2.11]$$

where, $|\rho| = \sqrt{x^2 + y^2}$ is the magnitude and the phase is given by:

$$\phi = tan^{-1}(y/x) \quad [2.12]$$

Figure 2.3 shows the complex representation of a vector ρ in the x-y plane.

For MRI, from Eq. 2.1, the frequency ω_0 of the spins placed in external magnetic field $\vec{B}_0$ is γB_0. In practice, the magnetic field is not perfectly homogeneous, there is the presence of local field $B(\vec{r})$. Thus, when taking into account the field inhomogeneity, the phase accumulated at time (t) can be rewritten as: (right-handed system)

$$\phi(\vec{r}, t) = -\gamma(B_0 - B(\vec{r}))t$$

or, $$\phi(\vec{r}, t) = -\gamma \cdot \Delta B(\vec{r}) \cdot t \quad [2.13]$$

where $\Delta B(\vec{r})$ represents the field variation induced by inhomogeities of the main magnetic field, susceptibility differences in the tissues in the human body and chemical-shift.

In a GRE acquisition, at t=TE, with any flow induced effects compensated, the accumulated phase for a right-handed system can be written as [1, 2]:

$$\phi(\vec{r}, TE) = -\gamma \Delta B(\vec{r}) \cdot TE + \phi_0(\vec{r}) \quad [2.14]$$

where $\phi_0(\vec{r})$ is the time-independent phase offset, related to local conductivity and permittivity.

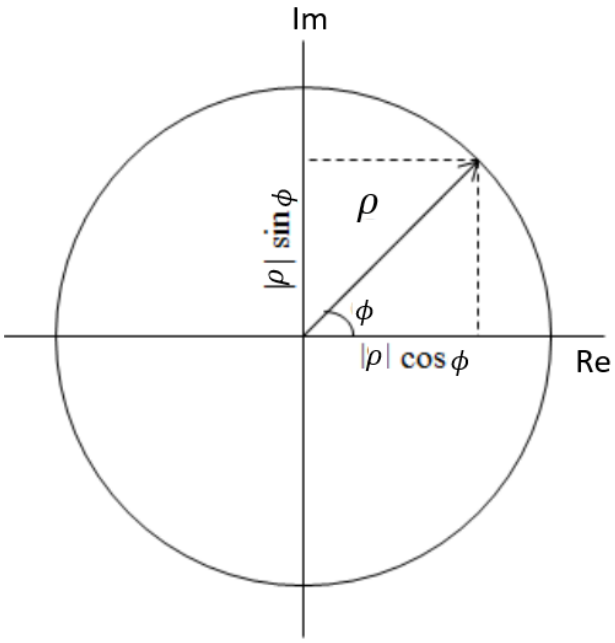

Figure 2.3 Complex representation of a vector ρ in the x-y plane. $|\rho|$ represents the magnitude and ϕ is the phase.

The operation of Eq. 2.12 can only return a phase value within the range of $-\pi$ to π. However, the true value of phase may be outside this range and the measured phase will be wrapped back into the range of $-\pi$ to π which is called phase aliasing. This wrapping process can be described as:

$$\phi_{wrapped}(\vec{r}) = \phi_{true}(\vec{r}) + 2\pi \cdot n(\vec{r}) \quad [2.15]$$

where the values of the function $n(\vec{r})$ are integers. In order to utilize the phase information without discontinuities, $\phi_{true}(\vec{r})$ is obtained through phase unwrapping.

2.4 Magnetic susceptibility

Magnetic susceptibility can be defined as the property of a substance, when placed within an external uniform magnetic field, which measures its tendency to get magnetized and alter the magnetic field around it [2].

When a substance is placed in an external magnetic field given by:

$$\vec{B} = \mu\vec{H} \quad [2.16]$$

where μ is the permeability and $\vec{H}$ is measured in Ampere/meter (A/m).

The actual magnetic field $\vec{B}$ inside the material can be written as:

$$\vec{B} = \mu_0(\vec{H} + \vec{M}) \quad [2.17]$$

where $\mu_0 = 4\pi\times10^{-7}\ Tm/A$ is the permeability of vacuum an $\vec{M}$ is the induced magnetization related to the $\vec{H}$ field. $\vec{M}$ can be written as:

$$\vec{M} = \chi \cdot \vec{H} \qquad [2.18]$$

where χ is the magnetic susceptibility of this substance.

Eq. 2.17 provides the expression for an induced magnetic field in presence of the external magnetic field and the induced magnetization for a given substance with susceptibility χ [2]. Equation 2.17 can be written as:

$$\vec{B} = \mu_0(1+\chi)\vec{H}$$

or,
$$\vec{B} = \mu_0(\tfrac{1+\chi}{\chi})\vec{M} \qquad [2.19]$$

Based on the magnetization they induced, the materials can be categorized as paramagnetic, diamagnetic and ferromagnetic materials. For paramagnetic materials, the induced magnetic moments are parallel to the external magnetic field, while for diamagnetic materials the induced moments are anti-parallel to the external field. For ferromagnetic materials, they can achieve saturation magnetization even at room temperature.

χ is positive for paramagnetic materials and is negative for diamagnetic materials. In MRI studies, the susceptibility of water (approximately -9 ppm relative to vacuum) is commonly used as the reference of susceptibility [2]. Thus, in the following chapters of this thesis, "paramagnetic" means that less diamagnetic than water (paramagnetic relative to water) while "diamagnetic" means more diamagnetic than water (diamagnetic relative to water).

Note that, as an important tissue in human body, blood has a unique susceptibility property. Blood is a composite substance that constitutes mainly the red blood cells and plasma. The susceptibility of a red blood cell depends on the oxygen saturation of hemoglobin within it. Ignoring the dissolved oxygen in plasma which has a slight paramagnetic susceptibility, the susceptibility of whole blood can be approximated as [2]:

$$\chi_{whole\ blood} = Hct\big(Y \cdot \chi_{oxy} + (1 - Y) \cdot \chi_{deoxy}\big) + (1 - Hct) \cdot \chi_{plasma} \quad [2.20]$$

where Hct represents hematocrit, which is the volume fraction of red blood cells in whole blood, χ_{plasma} is the susceptibility of plasma, and χ_{oxy} and χ_{deoxy} are the susceptibilities of a red blood cell with 100% ($Y = 1$, fully oxygenated) and 0% ($Y = 0,$ fully deoxygenated) oxygen saturation, and their susceptibility difference has been measured to be $2.62\ ppm$ per unit hematocrit [2]. Assuming that the susceptibility of fully oxygenated blood is approximately equal to the susceptibility of the surrounding tissue, the susceptibility difference between a blood vessel and surrounding tissue can be written as [2]:

$$\chi_{blood,relative} = \chi_{whole\ blood} - \chi_{tissue} = Hct \cdot (1 - Y) \cdot 2.62\ ppm \quad [2.21]$$

2.5 Predicting field variation through forward modeling and quantifying susceptibility as an inverse problem

As described in the previous section, when an object with susceptibility χ is placed in an external magnetic field $\vec{B}$, the actual field inside the object can be written as: (assuming $\chi \ll 1$)

$$\vec{B} = \mu_0(\frac{1+\chi}{\chi})\vec{M} \approx \mu_0\vec{M}/\chi \quad [2.22]$$

The induced magnetization $\vec{M}$ will generate a dipole field. Assuming that the external magnetic field is along the z direction, thus, only the z-components of the dipole field and $\vec{M}$ is considered in the following calculations. This z-component of the field variation can be written as:

$$\Delta B(\vec{r}) = \frac{\mu_0}{4\pi}\int_{V'} d^3r' \left\{\frac{3M_z(\vec{r}\prime)(z-z')^2}{|\vec{r}-\vec{r}\prime|^5}\right\} - \frac{M_z(\vec{r}\prime)}{|\vec{r}-\vec{r}\prime|^3} \quad [2.23]$$

this can be written as a convolution between $M_z(\vec{r})$ and the point-dipole response $G(\vec{r})$:

$$\Delta B_z(\vec{r}) = \mu_0 M_z(\vec{r}) * G(\vec{r}) \quad [2.24]$$

The Green's function $G(\vec{r})$ is given by:

$$G(\vec{r}) = \frac{1}{4\pi} \cdot \frac{3cos^2\theta - 1}{r^3} \quad [2.25]$$

where θ is the angle between $\vec{r}$ and $\vec{z}$. Particularly, $cos^2\theta = \frac{z^2}{r^2}$.

From Eqs. 2.22 to 2.25, the induced magnetic field variation can be predicted as:

$$\Delta B_z(\vec{r}) = \mu_0 M_z(\vec{r}) * G(\vec{r}) \approx B_0\chi(\vec{r}) * G(\vec{r}) \quad [2.26]$$

In Fourier domain, the convolution in Eq. 2.26 can be rewritten as:

$$\Delta B_z(\vec{r}) = B_0 \cdot FT^{-1}\{FT[\chi(\vec{r})] \cdot FT[G(\vec{r})]\} \quad [2.27]$$

where FT and FT^{-1} represent the Fourier transform and the inverse Fourier transform, respectively.

Additionally, the Fourier transform of $G(\vec{r})$ is given by:

$$G(\vec{k}) = FT[G(\vec{r})] = \begin{cases} \frac{1}{3} - \frac{k_z^2}{k_x^2+k_y^2+k_z^2}, & for\ \vec{k} \neq 0 \\ 0, & for\ \vec{k} = 0 \end{cases} \quad [2.28]$$

Thus, the induced field variation can be predicted using Eqs. 2.26 to 2.28. This process is referred to as the "forward modeling process" [3].

The field variation $\Delta B_z(\vec{r})$ can be obtained from phase images $\phi(\vec{r})$ using Eq. 2.14, and the susceptibility distribution $\chi(\vec{r})$ can be predicted from $\Delta B_z(\vec{r})$ using Eqs. 2.26 to 2.28. Although this calculation is not perfect, the results are considered to be reasonably good when the size of the object is much smaller than the field-of-view [3].

Eq. 2.27 indicates that the susceptibility distribution $\chi(\vec{r})$ can be predicted from the induced local field variations by solving the inverse problem. However, the zero values of $G(\vec{k})$ along the magic angle in the Fourier domain makes this estimation an ill-posed inverse problem. Thus, in order to generate a reliable estimate of $\chi(\vec{r})$, the methods used for solving the ill-posed inverse problem is of great interest. In the past few years, several algorithms have been proposed to solve this ill-posed inverse problem [3, 4].

(1) Single orientation methods

If the data is collected from a single orientation acquisition, the inverse problem could be solved through defining a k-space truncation threshold. For this approach, a regularized inverse filter is constructed, defined as [3]:

$$G'^{-1}(\vec{k}) = \begin{cases} \left(\frac{1}{3} - \frac{k_z^2}{k^2}\right)^{-1}, & for \ \left|\frac{1}{3} - \frac{k_z^2}{k^2}\right| > th \\ sgn\left(\frac{1}{3} - \frac{k_z^2}{k^2}\right)\left(\frac{1}{3} - \frac{k_z^2}{k^2}\right)^2 th^{-3}, & for \ \left|\frac{1}{3} - \frac{k_z^2}{k^2}\right| \leq th \end{cases} \quad [2.29]$$

where sgn refers to signal and th refers to the threshold. And $\chi(\vec{r})$ can be calculated as:

$$\chi(\vec{r}) = FT^{-1}\{G'^{-1}(\vec{k})FT[\Delta B_z(\vec{r})]\}/B_0 \quad [2.30]$$

Another single orientation method is known as optimization methods. For this method, $\chi(\vec{r})$ is calculated as:

$$argmin_{\chi(\vec{r})}\{\left\|W\left(\Delta B_z(\vec{r}) - \chi(\vec{r}) * G(\vec{r})\right)\right\|_2^2 + \lambda \cdot R(\chi) \quad [2.31]$$

where W is a weighting function and $R(\chi)$ is the regularization term. λ is a parameter that can be altered according to different purposes.

(2) Multiple orientation methods

By collecting the data with multiple orientations of the subject to the main magnetic field direction, the ill-posed inverse problem can also be solved [3, 4]. A method known as "calculation of susceptibility through multiple orientation sampling" (COSMOS) utilizes phase information from multiple orientations [5]. With three or more independent object orientations, COSMOS is able to solve the ill-posed inverse problem by combing the phase data from different orientations. This method is able to generate susceptibility maps that have almost no streaking artifacts. However, this method requires collecting data from at least three different orientations which increases the scan time. Thus, for routine *in vivo* brain imaging, multiple orientation acquisition is not practical due to the long scan time and required rotation of the head [3, 5].

2.6 QSM data processing steps

2.6.1 Single channel data combination

In practice, the combination of the complex data from different channels of phased array coils is the first and very important step for QSM reconstructions. Due to coil-sensitivity, phase images from different channels may have different phase offsets [3]. If not properly handled, the phase offsets will lead to open-ended fringe lines (also known as cusp artifacts) in combined phase images that will induce artifacts in the resultant susceptibility maps. One dataset that has cusp artifacts is shown in Chapter 4. Currently, there are mainly four types of multi-channel phase data combination algorithms including: (1) High-pass filtering method [3, 6], (2) Phase difference method [3, 7]. (3) Global phase offset correction method [3, 8]. (4) Coil-sensitivity correction method [3, 7].

2.6.2 Phase unwrapping

As discussed in previous sections, original phase images usually have phase aliasing, thus, phase unwrapping is an essential step for obtaining the true phase information. Phase unwrapping algorithms can be categorized as two types including spatial domain algorithms and temporal domain algorithms [3]. For spatial domain phase unwrapping methods, the key assumption is that the phase varies smoothly throughout the images, thus, the phase difference between neighboring pixels should be less than π. Several algorithms have been developed, such as image quality guided phase unwrapping [9], Laplacian based algorithms [10]. For temporal domain phase unwrapping methods, phase images acquired from at least three echo times (TEs) are required [3], and the TE increments between

neighboring echoes should be short in order to keep the phase increments as small as possible, thus, phase aliasing can be largely avoided in these phase increments [3]. This method offers pixel-by-pixel phase unwrapping with short processing time. Catalytic Multiecho Phase Unwrapping Scheme (CAMPUS) [11] is one of the temporal domain phase unwrapping methods. In case of atherosclerotic plaque with high susceptibility, the true phase difference between the plaque and the surrounding tissue may be greater than π, and the size of the plaque is rather small (a few pixels), spatial domain phase unwrapping method may fail here. However, temporal domain phase unwrapping method, such as CAMPUS that uses multi-echo phase data may still provide reliable unwrapped results. The algorithms of CAMPUS are discussed in Chapter 4.

2.6.3 Generating masks

After phase unwrapping, another important step is to generate the binary mask defining the region of interest for background field removal and QSM reconstruction. The regions with unreliable phase values (for example, regions near air-tissue interfaces) will usually induce errors and severe streaking artifacts in the resultant susceptibility maps [3, 4]. Thus, removing all the noisy regions is of great importance.

2.6.4 Background field removal

From Eq. 2.14, the field variation can be extracted from the phase images. In practice, this extracted field variation can be considered as a combination of the background field $\Delta B_b(\vec{r})$ and local field $\Delta B_l(\vec{r})$:

$$\Delta B_z(\vec{r}) = \Delta B_b(\vec{r}) + \Delta B_l(\vec{r}) \quad [2.32]$$

The background field is induced by the field inhomogeneities, air/tissue interfaces, and global geometry. The local field variation $\Delta B_l(\vec{r})$ is induced by the local susceptibility distribution, thus, only $\Delta B_l(\vec{r})$ is of interest in QSM [3]. To date, several approaches have been developed for background field removal including: (i) the sophisticated harmonic artifact reduction for phase data (SHARP) method [12], (ii) the projection onto dipole fields (PDF) method [13], and (iii) high-pass filtering method [14].

SHARP is based on the assumption that the background field is a harmonic function while the local field is assumed not to be harmonic [3]. The spherical mean value property of the background field can be understood by:

$$\Delta B_b(\vec{r}) = \Delta B_b(\vec{r}) * s \quad [2.33]$$

where s is a normalized spherical kernel, thus,

$$\Delta B'(\vec{r}) = \Delta B_z(\vec{r}) - \Delta B_z(\vec{r}) * s = \Delta B_l(\vec{r}) - \Delta B_l(\vec{r}) * s \quad [2.34]$$

The signal of the local field variation may be partially removed by the spherical filtering process, thus, as a final step, the signal loss can be compensated by a deconvolution process [3]:

$$\Delta B_l(\vec{r}) = \Delta B'^{(\vec{r})} * (\delta - s)^{-1} \quad [2.35]$$

where $(\delta - s)^{-1}$ is the regularized inverse kernel.

SHARP has been demonstrated the ability to remove the background field effectively. However, in practice, even a small phase aliasing on the input phase image will lead to a larger artifact after SHARP filtering. Thus, the regions that have phase aliasing or abnormalities need to be removed by applying the mask before SHARP filtering.

2.6.5 Solving the ill-posed inverse problem

As discussed in the previous section, there are various algorithms have been proposed for solving this ill-posed inverse problem including single orientation methods (e.g. truncated k-space division method [3]) and multiple orientation methods (e.g. COSMOS method [5]). The QSM data processing procedures are illustrated in **Fig. 2.4**.

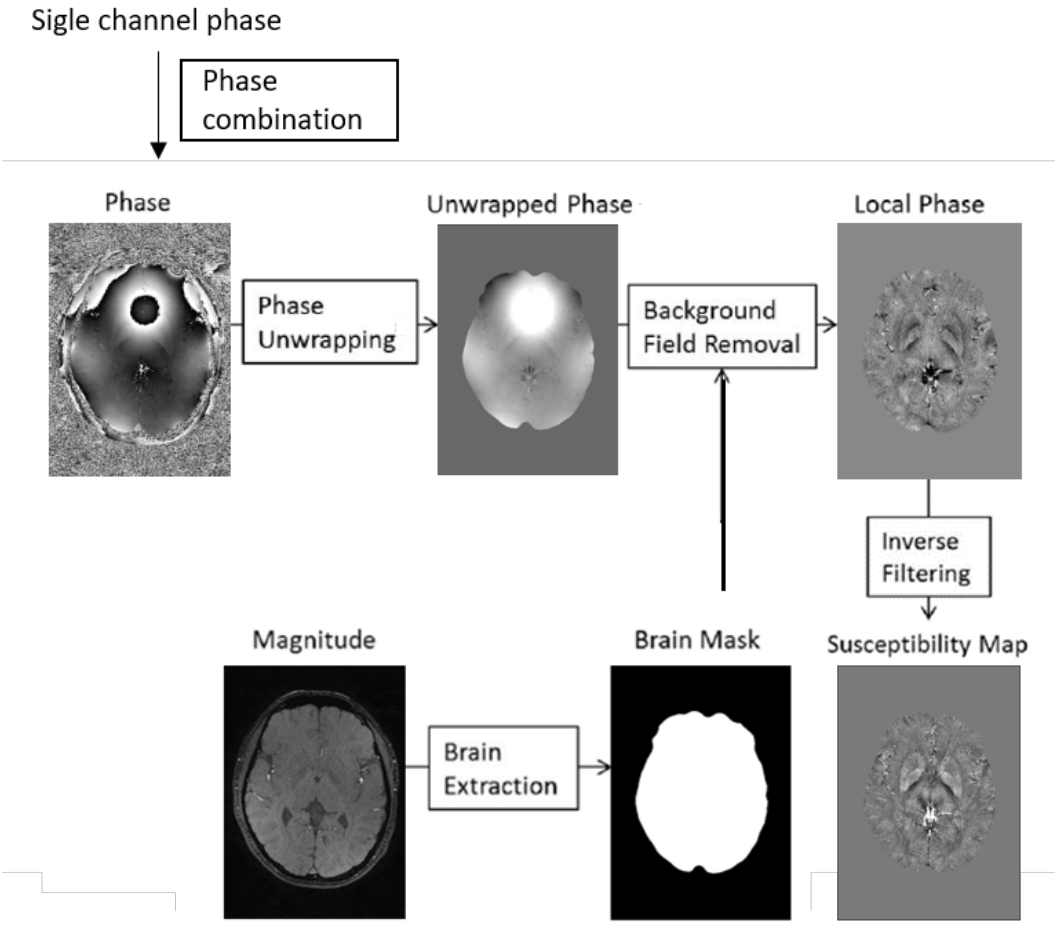

Figure 2.4 QSM data processing procedures. The dashed line indicates that brain masks may not be required for phase unwrapping.

References

1. Haacke EM, Brown RW, Thompson MR, Venkatesan R. Magnetic Resonance Imaging: Physical Principles and Sequence Design. 1st ed. Wiley-Liss; 1999.

2. Haacke EM, Reichenbach JR, editors. Susceptibility Weighted Imaging in MRI: Basic Concepts and Clinical Applications. 1st ed. Wiley-Blackwell; 2011.

3. Haacke EM, Liu S, Buch S, Zheng W, Wu D, Ye Y. Quantitative susceptibility mapping: current status and future directions. Magn. Reson. Imaging 2015; 33(1): 1–25.

4. Deistung, Andreas, Ferdinand Schweser, and Jürgen R. Reichenbach. Overview of quantitative susceptibility mapping. NMR in Biomedicine (2016).

5. Liu T, Spincemaille P, de Rochefort L, Kressler B, Wang Y. Calculation of susceptibility through multiple orientation sampling (COSMOS): a method for conditioning the inverse problem from measured magnetic field map to susceptibility source image in MRI. Magn. Reson. Med. 2009; 61(1): 196–204. 100. Wharton S, Bowtell R. Whole-brain

6. Koopmans PJ, Manniesing R, Niessen WJ, Viergever MA, Barth M. MR venography of the human brain using susceptibility weighted imaging at very high field strength. MAGMA 2008;21(1–2):149–58.

7. Robinson S, Grabner G, Witoszynskyj S, Trattnig S. Combining phase images from multi-channel RF coils using 3D phase offset maps derived from a dualecho scan. Magn Reson Med 2011;65(6):1638–48.

8. Hammond KE, Lupo JM, Xu D, Metcalf M, Kelley DAC, Pelletier D, et al. Development of a robust method for generating 7.0 T multichannel phase images of the brain with

application to normal volunteers and patients with neurological diseases. NeuroImage 2008;39(4):1682–92.

9. Witoszynskyj S, Rauscher A, Reichenbach JR, Barth M. Phase unwrapping of MR images using ΦUN–a fast and robust region growing algorithm. Med Image Anal 2009;13(2):257–68.

10. Schofield MA, Zhu Y. Fast phase unwrapping algorithm for interferometric applications. Opt Lett 2003;28(14):1194–6.

11. Feng W, Neelavalli J, Haacke EM. Catalytic multiecho phase unwrapping scheme (CAMPUS) in multiecho gradient echo imaging: removing phase wraps on a voxel-by-voxel basis. Magn Reson Med 2013;70(1):117–26.

12. Schweser F, Deistung A, Lehr BW, Reichenbach JR. Quantitative imaging of intrinsic magnetic tissue properties using MRI signal phase: an approach to in vivo brain iron metabolism? NeuroImage 2011;54(4):2789–807.

13. Liu T, Khalidov I, de Rochefort L, Spincemaille P, Liu J, Tsiouris AJ, et al. A novel background field removal method for MRI using projection onto dipole fields (PDF). NMR Biomed 2011;24(9):1129–36.

14. Haacke EM, Xu Y, Cheng YN, Reichenbach JR. Susceptibility weighted imaging (SWI). Magn Reson Med 2004;52(3):612–8.

Chapter 3. Carotid Atherosclerotic Plaque Imaging

Atherosclerotic disease is the leading cause of death and disability worldwide [1]. Outside of the coronary arteries, the carotid arteries are likely the most clinically significant site of atherosclerosis. Carotid atherosclerosis is considered to be response for as many as 20% of all ischemic strokes cases [1]. The close relationship between carotid atherosclerosis and ischemic stroke led to more than one million carotid endarterectomy (CEA) and carotid artery stenting (CAS) procedures performed on high risk patients from 1998 to 2008 in the United States [2].

In current clinical practice, the diagnosis or assessment of carotid atherosclerosis is based on the risk of stroke. Previously, the percentage of stenosis of the vessel blocked by the atherosclerotic plaque was a primary indicator for the risk of atherosclerotic plaque [1]. However, recent studies have shown that patients without any measurable stenosis might have advanced plaques features that will also lead to high risk of stroke [3]. Thus, basing decisions solely on the degree of stenosis will lead to misestimation of the patients' risk of stroke and this has led to an increasing interest in assessing the high-risk features of atherosclerotic plaque [3]. To date, numerous studies have been dedicated to identifying additional high-risk features of carotid atherosclerosis.

To better study the atherosclerotic plaques, a robust high-resolution imaging method that is able to visualize plaque morphology, detect high-risk features associated with the plaque is of great interest. Thus, magnetic resonance imaging (MRI) is emerging as the best candidate due to its excellent soft tissue contrast and non-invasive 3D capabilities that enables the direct visualization and characterization of the atherosclerotic plaque lesions [1].

3.1 Lesion types for atherosclerotic plaques and the concept of vulnerable plaques

3.1.1. Atherosclerotic plaque classification

Numerous studies have proven that a simple assessment of luminal stenosis has limited clinical value in predicting the risk of atherosclerotic plaque [3]. Thus, identifying atherosclerotic plaque compositions and structure is of great importance, a classification scheme for atherosclerotic plaque has been created by the American Heart Association (AHA) that was designed to be used as a histological “template” for images obtained in the clinical settings [4]. Cai et al. subsequently modified the AHA classification to adapt MR imaging due to its lack of abilities to differentiate several plaque features [5]. The modified the AHA classification is shown in **Table 3.1**.

Table 3.1 Modified AHA classification of atherosclerotic plaque for MRI [5]

Modified AHA Classification for MRI
Type 1: near-normal wall thickness with no calcification
Type 2: thickening wall or small plaque with no calcification
Type 3: plaque with a lipid necrotic core surrounded by fibrous tissue with possible calcification
Type 4: complex plaque with possible surface defect, hemorrhage, or thrombus
Type 5: calcified plaque
Type 6: fibrotic plaque without lipid core and with possible small calcifications

3.1.2. The concept of vulnerable plaques

The presence of carotid Atherosclerotic plaques can be categorized into two types, one is the stable plaques that progress over time and restrict blood flow *in situ*, the other one is the plaques that are likely to rupture leading to thrombosis *in situ* or the ruptured plaque travels with blood flow to block smaller arteries in brain, thus, cause ischemic stroke. [6]. Over the years, a few terms have been used to define the latter type, such as “unstable plaque”, “high-risk plaque”, and “vulnerable plaque” etc. To provide a uniform language to help standardize the terminology, a group of clinicians have recommended “vulnerable

plaque" to identify the plaque that has a high probability of undergoing rapid progression or future ruptures, thus causing ischemic events [6]. In this thesis, "vulnerable plaque" will be used as the terminology.

3.1.3. Criteria for Defining Vulnerable Plaque

Due to its clinical importance, numerous studies have been devoted to developing the criteria for defining vulnerable plaque, based on histological analysis, a list of major and minor criteria for defining vulnerable has been proposed by a group of clinicians [6]. Note that, these criteria are from *ex vivo* histological analysis, thus, a list of MRI detectable criteria has been summarized in this thesis including lipid-rich necrotic core (LRNC) with thin cap, intraplaque hemorrhage (IPH) and calcification. **Table 3.2** shows the major MRI detectable criteria.

Table 3.1 MRI detectable criteria for defining vulnerable plaque, based on the histological study [6]

MRI detectable criteria
• Thin cap with lipid-rich necrotic core (LRNC)
• Fissured plaque
• Stenosis > 90%
• Superficial calcified nodule
• Intraplaque hemorrhage (IPH)

i) Intraplaque Hemorrhage (IPH)

To date, the vulnerable feature that has drawn the most attention for its high stroke risk has been intraplaque hemorrhage (IPH). Results from numerous studies have demonstrated a consistent pattern of higher stroke rates for patients with IPH [1-7]. The development of IPH is thought to be the related to the immature and leaky neovessels that have vascularized the plaque [1, 8, 9]. Results from studies by Takaya et al. [10] and Underhill et al. [11] have shown that IPH accelerates the growth of carotid plaque. In an 18-month study of 29 asymptomatic patients with 50-79% stenosis, Takaya et al. identified a significant change in vessel wall and LRNC volume in subjects with IPH comparing with those without IPH [10]. IPH is also considered to be a proinflammatory stimulus which can lead to accumulations of macrophages that release proteinases, therefore, degrading the fibrous cap that will cause cap rupture [1, 12]. Rupture of the fibrous cap with subsequent thrombosis is one of the most important features of high-risk carotid plaques [1, 7].

MRI be can used to detect IPH due to the presence of methemoglobin, which can be considered as an endogenous contrast agent that has short longitudinal relaxation time (T1) comparing to the surrounding tissues, thus, area of IPH will show hyperintensity on T1-weighted images [1, 7]. Although areas of IPH will show bright on T1-weighted images, clinically, a combination of signals from different contrast weightings images (T1-weighted, T2-weighted, PD-weighted, etc.) are needed to be able to confidently identify IPH. However, another important property of IPH, the magnetic susceptibility changes due to the presence of iron, provides excellent contrast between IPH and the surrounding tissue. Thus, IPH can be identified solely based on QSM results, which is discussed in Chapter 4.

ii) Lipid-rich necrotic core (LRNC) and the status of fibrous cap (FC)

The lipid-rich necrotic core (LRNC) is defined as "a mixture of lipids and necrotic debris contained by a smooth, cell-rich fibrous cap" [1, 13]. Cholesterol and cholesterol esters are two principal components of LRNC [1]. In carotid arteries, a cap with thickness less than 200 μm is considered a thin cap and a lipid core that accounts greater than 40% of the plaque's total volume is considered a large lipid core [14]. The most common type of plaque disruption is caused by the rupture of the fibrous cap overlying the necrotic core, thus both large necrotic cores and thin fibrous caps are considered to have higher risk of plaque disruption and thus, cause ischemic events. Results from a study by Takaya et al. have proven this hypothesis [15]. Takaya et al. also found that fibrous cap thinning was likely to cause fibrous cap rupture [15]. Findings by Takaya et al. indicate that thin and ruptured

fibrous may have similar possibility to develop future ischemic events [15]. Thus, thin cap with LRNC is one of the major criteria for identifying vulnerable plaque.

A study reported by Underhill et al. scanned 85 patients with 50-79% stenosis and no plaque surface disruption at baseline, patients were imaged with contrast-enhanced carotid MRI [16]. Results from this study have shown that the size of the LRNC was the most significant indicator for development of a new surface disruption at the three-year follow-up scan [16]. Note that, this study has also shown that the presence of IPH was also a major indicator of new surface disruption [16]. These findings have demonstrated the importance of LRNC and IPH as two major criteria for identifying vulnerable plaque.

MRI can be used to detect the LRNC due to its short transverse relaxation time (T2) comparing with the surrounding tissues. Thus, areas of the LRNC can be detected as hypointense signal on T2-weighted images [17]. Because the fibrous cap in atherosclerotic plaques enhances with gadolinium-based contrast agents, while the LRNC, lacking both vasculature and matrix, shows no or very limited enhancement [1]. Thus, Cai et al. used contrast-enhanced (CE) T1-weighted MR imaging to detect the status of the fibrous cap [18]. Their results showed that the measured LRNC area and the status of fibrous cap using CE-MRI were strongly correlated with histology analysis [18]. Cai et al. results have demonstrated that CE-MRI is capable of measuring the fibrous cap and LRNC.

A typical treatment for atherosclerosis is lipid-lowering therapy [17]. Several studies have demonstrated that statin therapy reduces plaque burden in carotid atherosclerosis [1]. A clinical trial by Zhao et al. has shown that patients with LRNC (with no IPH) showed decreased size of LRNC after lipid depletion therapy, their findings have shown that statin therapy can specifically reduce the size of the LRNC [19].

iii) Plaque calcification

Calcification in atherosclerotic plaque is usually considered as an indicator of stable plaque that is not likely to develop future disruption [1]. However, in some cases, such as calcified nodule can lead to a weak structure of the plaque. Specifically, the interaction of calcified nodules and the lumen can cause thrombus [20]. In MRI, plaque calcification is characterized by defined areas with a hypointense signal on all 3 types of images (T1-weighted, T2-weighted, and PD-weighted images) [1].

3.2 Current MRI techniques for carotid atherosclerotic plaques imaging

As discussed in previous sections, a simple assessment of luminal stenosis for carotid atherosclerosis has limited clinical value in predicting the risk of ischemic stroke [3]. MRI should be able to not only visualize the presence of atherosclerosis but also detect vulnerable plaques features discussed in previous sections and ultimately, distinguish patients with high risk of stroke. MRI is one of the most promising modalities for carotid atherosclerosis imaging, as MR is capable of characterizing different lesion types of the plaque, and also can be used to monitor the progression of the disease.

To date, a 2D multi-contrast MRI method has been proposed as a protocol for plaque imaging [21]. This approach includes three basic contrast weightings (T1, T2, PD) obtainable with black-blood imaging technique and/or time of flight (TOF) images. In addition, contrast-enhanced MR imaging also has been used for carotid atherosclerosis imaging [21]. Numerous studies have shown that combined intensity information from different contrast weightings can be used to identify vulnerable plaque components, including fibrous tissue, lipid-rich necrotic core, calcification, and intraplaque hemorrhage [21].

Due to the fast blood flow circulating in carotid arteries, one essential requirement for MR carotid plaque imaging is flow suppression [22]. Over the years, numerous studies have been dedicated to develop effective flow suppression techniques for 2D carotid MRI. To

date, double inversion recovery technique and motion sensitization technique has been the two most popular and effective techniques [22].

3.2.1. Double inversion black-blood technique

Double inversion black-blood technique uses two inversion pluses to null signal from blood flow so it will show black on MR images [23]. **Figure 3.1** shows the mechanism of double inversion and a sequence diagram for spin echo with black-blood preparation.

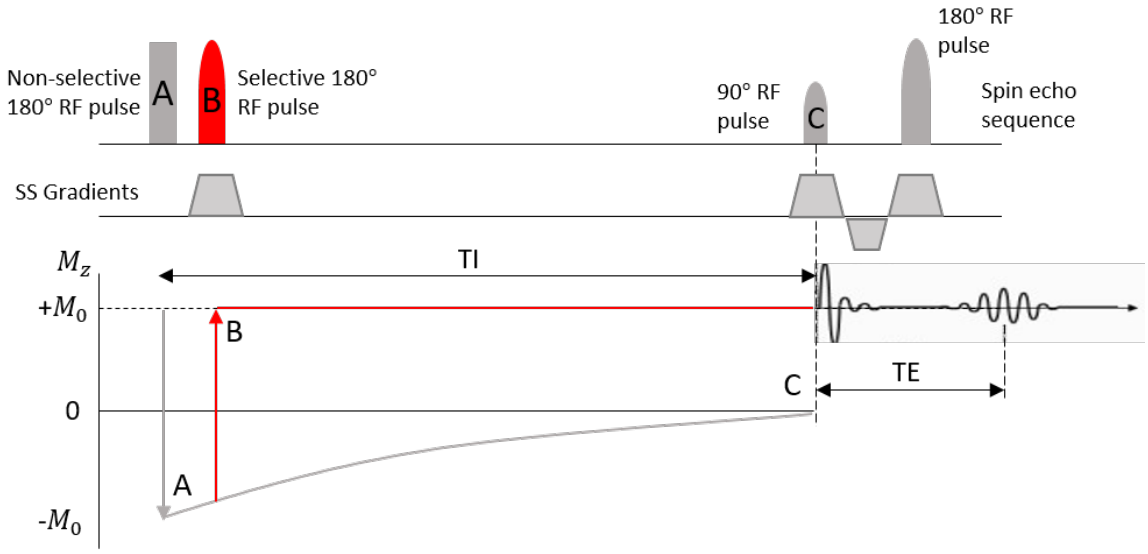

Figure 3.1 Double-inversion black-blood preparation sequence diagram

As shown in the above figure, double inversion preparation includes several steps:

i) a non-selective 180° pulse to excite all the slices. The magnetization M_z of the tissue excited by this pulse was inverted to $-M_0$

ii) a slice-selective 180° pulse to reset signal of the slice of interest, thus M_z of this slice was inverted back to M_0

iii) the blood flow with $M_z = M_0$ flows forward, while blood flow with $M_z = -M_0$ constantly flows into the slice plane

iv) after a delay (TI) the blood signal in the slice plane at that moment is nulled and the slice of interest is prepared for the following sequence, in this case, it is a spin echo sequence.

The results from turbo spin-echo (TSE) sequence with double inversion black-blood technique are shown in **Figure 3.2**. The signal of blood flow was nulled (showing black on images) while other stable tissues remain original contrast.

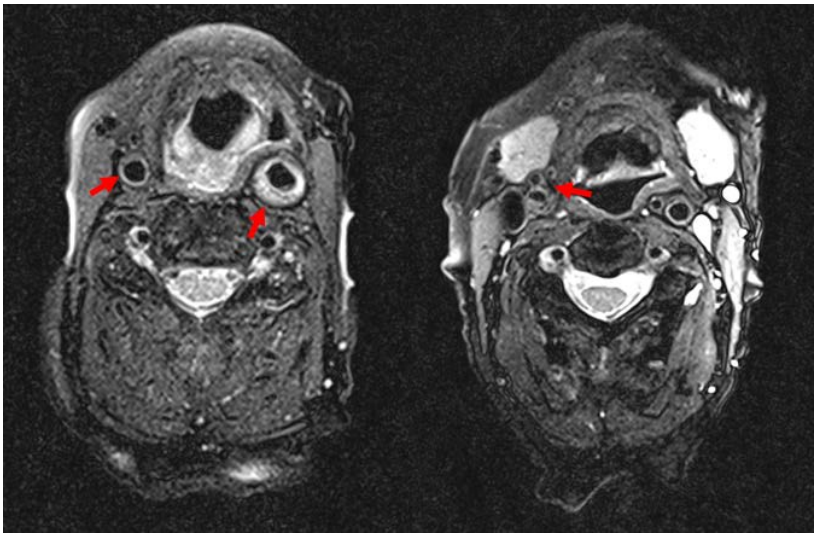

Figure 3.2 MR images from turbo spin-echo (TSE) sequence with double-inversion black-blood preparation. Red arrows identify the regions of dark blood, bright thickened vessel wall and carotid artery bifurcation.

3.2.2. Motion-sensitization black-blood technique

The motion-sensitization black-blood technique utilizes motion-sensitizing gradients to dephase all moving blood spins prior to imaging, it is called motion-sensitizing magnetization preparation (MSPREP) technique [24]. The preparation sequence consists of 90°-180°-90° non-selective RF pulses and a pair of identical unipolar gradients around the 180° pulse, as shown in **Figure 3.3**.

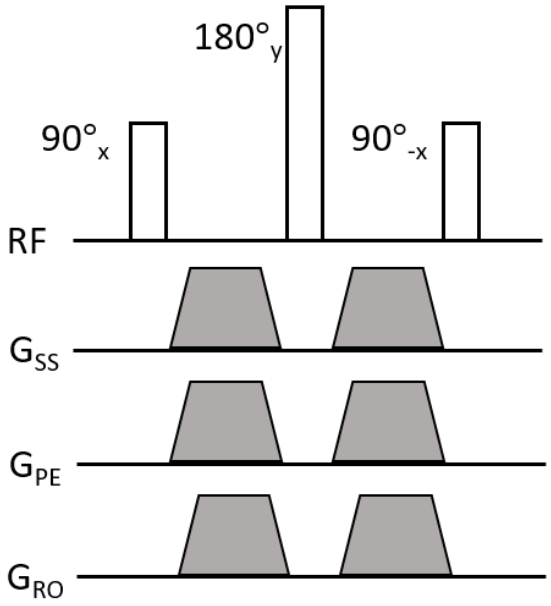

Figure 3.3 Illustration of the motion-sensitizing magnetization preparation (MSPREP) sequence. This MSPREP sequences includes 90_x tip-down, 180_y refocusing, and 90_{-x} tip-up nonselective RF pulses with motion-sensitizing gradients positioned around the 180_y pulse in all three directions.

The MSPREP sequence includes three consecutive rectangular RF pulses with flip angles of 90°, 180°, and 90°, and phases of 0°, 90°, and 180°, respectively [24]. Two identical motion-sensitizing gradient pulses are symmetrically placed around the 180° refocusing pulse and applied in all three orthogonal directions. The $180°_y$ refocusing pulse was used to minimize off-resonance effects, which will lead to signal loss of both stable and moving spins due to T2 decay. Moving tissues experience further signal loss due to the intravoxel dephasing [24].

For carotid MRI application, MSPREP can be applied with turbo spin-echo (TSE), gradient recalled echo (GRE), or steady-state free-precession (SSFP) readout. **Figure 3.4** is a sequence diagram for a TSE acquisition with MSPREP [25]. After motion-sensitization black-blood preparation, spoiler gradients are applied to destroy remnant transverse magnetization. A fat saturation module is placed after spoiler gradients to achieve fat suppression. The TSE sequence is placed after all preparation pulses and was used to acquire the data.

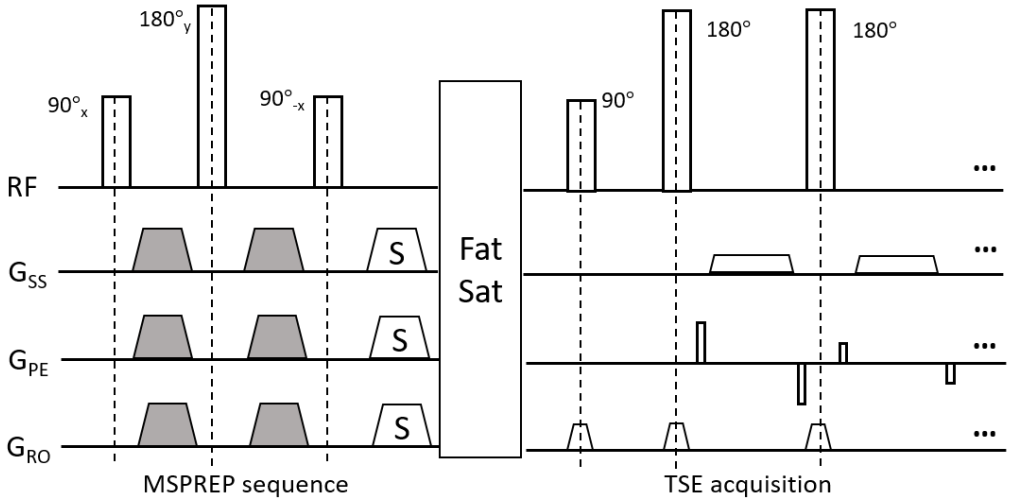

Figure 3.4 Illustration of the TSE-based MSPREP sequence. Preparation sequence includes: (1) MSPREP, (2) spoiler gradients, (3) a fat saturation module. TSE sequence was used for image acquisition.

3.2.3. 3D MRI techniques for carotid plaque imaging

Although well accepted, the 2D multi-contrast approach has a few shortcomings. For 2D imaging, the scan time can be long, the voxel size will not be isotropic, thus, the spatial information about the plaque may be missed, and the coverage of the neck is limited [22]. Thus, several 3D MRI techniques have been developed for carotid plaque imaging recently. Comparing with 2D imaging acquisition, 3D imaging acquisition in general, benefits from improved spatial resolution and SNR [22]. In addition, isotropic voxels will improve the accuracy of the measurement using carotid MR imaging [22]. Thus, numerous studies have been dedicated to develop 3D imaging methods for carotid atherosclerosis imaging. To date, several 3D methods have been proposed.

i) 3D Motion-Sensitized Driven Equilibrium Prepared Rapid GRE technique

The 3D motion-sensitized driven equilibrium prepared rapid gradient echo (MERGE) technique was introduced by Balu et al. in 2011 [22, 26]. It includes a flow-suppression preparation module called motion-sensitized driven equilibrium (MSDE) and a low flip angle gradient echo acquisition [22, 26].

ii) 3D Magnetization Prepared Rapid Acquisition Gradient Echo (MPRAGE) technique

3D magnetization prepared rapid acquisition gradient echo (MPRAGE) is a heavily T1-weighted technique and was proposed for carotid atherosclerosis imaging by Moody et at.

[22, 27]. As discussed in previous sections, due to its short T1, IPH can be detected as hyperintensity on the T1-weighted images. Thus, MPRAGE has great potential for imaging the IPH.

iii) 3D Turbo Spin Echo (TSE) technique

Fan et al. developed a technique called 3D SPACE (variable-flip-angle 3D TSE T2w) for carotid atherosclerosis imaging, which combined TSE with black blood technique and variable flip angle acquisition technique [22, 28].

3.3 Discussion and the future of carotid plaque imaging with quantitative susceptibility mapping (QSM) technique

In previous sections, the importance of identifying vulnerable plaque and current MRI techniques for carotid plaque imaging have been discussed. MRI strategies for imaging the vulnerable plaque focuses on identifying the status of fibrous cap, lipid-rich necrotic core (LRNC), intraplaque hemorrhage (IPH) and calcifications. Currently, the most popular approach for characterizing carotid plaque is multi-contrast MRI, using combined intensity information from T1-weighted, T2-weighted, PD-weighted and morphology information from MR images to differentiate and detect plaque compositions [21]. A tissue type classification scheme based on intensity information has been developed [1], as shown in **Table 3.3**.

Table 3.2 Scheme for identifying plaque components from different MRI contrast weightings [1]

Component	Contrast weighting			
	T1W	T2W	PDW	TOF
LRNC with IPH	$+$	$-/+$	$+$	$+$
LRNC without IPH	$0/+$	$-/0$	$0/+$	0
Calcification	$-$	$-$	$-$	$-$

$+$: hyperintense; 0: isointense; $-$: hypointense.

This scheme can be interpreted as:

1. The LRNC is generally located in the bulk of the plaque and is isointense to hyperintense on T1-weighted and PD-weighted images [1].

2. IPH are identified by (i) fresh hemorrhage appears as a hyperintense signal on T1-weighted and TOF images and as an isointense signal on T2-weighted and PD-weighted images. Recent hemorrhage is identified by a hyperintense signal on all 4 contrast weightings. [1].

3. Calcification is identified by areas with hypointense signals on all 4 images with different weightings [1].

In summary, the most critical indicators for vulnerable plaque are the status of fibrous cap, IPH, and calcification. Thin or ruptured fibrous cap and IPH indicate the vulnerability of the atherosclerotic plaque while large calcification usually indicates stable plaque, however, calcified nodule can contribute to risk of disruption. Calcified nodules can be distinguished from most plaque calcifications by its morphology, because stable calcifications are separated from the lumen [1]. In another word, these criteria are differentiated by morphology (the status of fibrous cap and calcified nodules) and intensity information (IPH and calcification). However, Table 3.4 has shown that identifying IPH and calcification needs intensity information from at least four different contrast weightings, clearly, accuracy and sensitivity can be a problem with this multi-contrast MRI approach.

Current carotid MRI techniques are all based on magnitude information and are hampered by the limitations of magnitude images. However, phase information can provide better contrast between hemorrhage and calcification. The QSM techniques that utilize phase information, as discussed in Chapter 2, has been widely used as a tool for quantifying the tissue susceptibility in the brain, such as the quantification of cerebral iron deposition or calcium [30]. The susceptibility contrast is extremely sensitive to hemorrhage and calcium which makes QSM a potential tool for carotid plaque imaging as a means to identifying IPH and calcification.

Combining QSM with current magnitude based techniques is promising. Magnitude based techniques can be used to obtain morphology information, such as the location of plaque,

the size of the stenosis, and the status of fibrous cap. Susceptibility maps can provide information on the components of the plaque, such as IPH and calcification instead of acquiring all four contrast weightings data. More technical details of implementing carotid QSM will be discussed in the following chapter.

References

1. Kerwin, William S. Carotid artery disease and stroke: assessing risk with vessel wall MRI. ISRN cardiology 2012 (2012).

2. T.M. Dumont and A. I. Rughani, National trends in carotid artery revascularization surgery: clinical article. Journal of Neurosurgery, vol. 116, no. 6, pp. 1251–1257, 2012.

3. Saam, T., et al. Quantitative evaluation of carotid plaque composition by in vivo MRI. Arteriosclerosis, thrombosis, and vascular biology 25.1 (2005): 234-239.

4. Stary HC. Natural history and histological classification of atherosclerotic lesions. Arterioscler Thromb Vasc Biol. 2000;20:1777–1778.

5. Cai, Jian-Ming, et al. Classification of human carotid atherosclerotic lesions with in vivo multicontrast magnetic resonance imaging. Circulation 106.11 (2002): 1368-1373.

6. Naghavi, Morteza, et al. From vulnerable plaque to vulnerable patient a call for new definitions and risk assessment strategies: part I. Circulation 108.14 (2003): 1664-1672.

7. Kerwin, William S. "Carotid artery disease and stroke: assessing risk with vessel wall MRI." ISRN cardiology 2012 (2012).

8. F. D. Kolodgie, H. K. Gold, A. P. Burke et al. Intraplaque hemorrhage and progression of coronary atheroma. The New England Journal of Medicine, vol. 349, no. 24, pp. 2316–2325, 2003.

9. R. Virmani, F. D. Kolodgie, A. P. Burke et al. Atherosclerotic plaque progression and vulnerability to rupture: angiogenesis as a source of intraplaque hemorrhage. Arteriosclerosis, Thrombosis, and Vascular Biology, vol. 25, no. 10, pp. 2054– 2061, 2005.

10. Takaya, Norihide, et al. "Presence of Intraplaque Hemorrhage Stimulates Progression of Carotid Atherosclerotic Plaques A High-Resolution Magnetic Resonance Imaging Study." Circulation 111.21 (2005): 2768-2775.

11. Underhill, Hunter R., et al. Arterial remodeling in the subclinical carotid artery disease. JACC: Cardiovascular Imaging 2.12 (2009): 1381-1389.

12. A. V. Finn, M. Nakano, R. Polavarapu et al. Hemoglobin directs macrophage differentiation and prevents foam cell formation in human atherosclerotic plaques. Journal of the American College of Cardiology, vol. 59, no. 2, pp. 166–177, 2012.

13. Virmani, Renu, et al. "Lessons from sudden coronary death a comprehensive morphological classification scheme for atherosclerotic lesions." Arteriosclerosis, thrombosis, and vascular biology 20.5 (2000): 1262-1275.

14. J. N. Redgrave, P. Gallagher, J. K. Lovett, and P. M. Rothwell. Critical cap thickness and rupture in symptomatic carotid plaques: the oxford plaque study. Stroke, vol. 39, no. 6, pp. 1722–1729, 2008.

15. Takaya, Norihide, et al. Association between carotid plaque characteristics and subsequent ischemic cerebrovascular events. Stroke 37.3 (2006): 818-823.

16. Underhill, H. R., et al. Predictors of surface disruption with MR imaging in asymptomatic carotid artery stenosis. American Journal of Neuroradiology 31.3 (2010): 487-493.

17. Underhill, Hunter R., et al. MRI of carotid atherosclerosis: clinical implications and future directions. Nature Reviews Cardiology 7.3 (2010): 165-173.

18. Cai J, et al. In Vivo Quantative Measurement of Intact Fibrous Cap and Lipid Rich Necrotic Core Size in Atherosclerotic Carotid Plaque: A Comparison of High Resolution Contrast Enhanced MRI and Histology. Circulation. 2005

19. Zhao, X. Q., et al. Magnetic resonance imaging of the plaque lipid depletion during lipid therapy: a prospective assessment of efficacy and time-course. A late breaking clinical trial report at ACC (2009): 28-31.

20. R. Virmani, E. R. Ladich, A. P. Burke, and F. D. Kolodgie, "Histopathology of carotid atherosclerotic disease," Neurosurgery, vol. 59, no. 5, pp. S219–S3, 2006.

21. Yuan, Chun, et al. MRI of carotid atherosclerosis. Journal of nuclear cardiology 15.2 (2008): 266-275.

22. Yuan, Chun, and Dennis L. Parker. Three-Dimensional Carotid Plaque MR Imaging. Neuroimaging Clinics of North America 26.1 (2016): 1-12.

23. Edelman RR, Chien D, Kim D. Fast selective black blood MR imaging. Radiology 1991;181(3):655–60.

24. Nguyen, Thanh D., et al. Effective motion-sensitizing magnetization preparation for black blood magnetic resonance imaging of the heart. Journal of Magnetic Resonance Imaging 28.5 (2008): 1092-1100.

25. Wang, Jinnan, et al. Improved suppression of plaque-mimicking artifacts in black-blood carotid atherosclerosis imaging using a multislice motion-sensitized driven-equilibrium (MSDE) turbo spin-echo (TSE) sequence. Magnetic resonance in medicine 58.5 (2007): 973-981.

26. Balu N, Yarnykh V, Chu B, et al, editors. Carotid plaque assessment using fast 3D isotropic-resolution black-blood MRI. International Society of Magnetic Resonance in Medicine; 2009.

27. Moody AR, Murphy RE, Morgan PS, et al. Characterization of complicated carotid plaque with magnetic resonance direct thrombus imaging in patients with cerebral ischemia. Circulation 2003;107(24):3047–52.

28. Zhang Z, Fan Z, Carroll TJ, et al. Three-dimensional T2-weighted MRI of the human femoral arterial vessel wall at 3.0 Tesla. Invest Radiol 2009;44(9): 619–26.

29. Yim YJ, Choe YH, Ko Y, et al. High signal intensity halo around the carotid artery on maximum intensity projection images of time-of-flight MR angiography: a new sign for intraplaque hemorrhage. J Magn Reson Imaging 2008;27(6):1341–6.

30. Haacke, E. Mark, et al. "Quantitative susceptibility mapping: current status and future directions." Magnetic resonance imaging 33.1 (2015): 1-25.

Chapter 4. Quantitative Susceptibility Mapping of Atherosclerosis in Carotid Arteries

4.1 The water/fat chemical shift

As an important physical phenomenon, chemical shift is similar to magnetic susceptibility in its electronic nature of origin, but has a different macroscopic effect in MR imaging [1, 2]. Different from magnetic susceptibility, chemical shift does not induce a magnetization in the subject when it is placed in an external magnetic field [1, 2]. However, being more local and time-related, it involves the interaction of the electrons within a molecule and/or between neighboring molecules which causes a uniform and finite shift in the magnetic field experienced by certain nuclei within the molecule [2].

For example, protons in water (H_2O) see a different field from those in a lipid-based or fatty compound (which contains CH_2 and CH_3). The 'water' signal (from water-bearing material or tissue) while the latter represents the 'fat' signal [1, 2]. The difference between their precession frequencies $\Delta\omega_{fw}$ is given by:

$$\Delta\omega_{fw} = \omega_f - \omega_w = -\sigma_{fw}\gamma B_0 \quad [4.1]$$

where the suffix w stands for water, f for fat, σ_{fw} (a positive quantity in this case) is the chemical shift between water and fat, and $\Delta\omega_{fw}$ refers to the frequency shift of fat relative to water. Most fat in the human body has $\sigma_{fw} = 3.5\ ppm$ [1, 2]. **Fig. 4.1** is an illustration of water/fat spectral peaks.

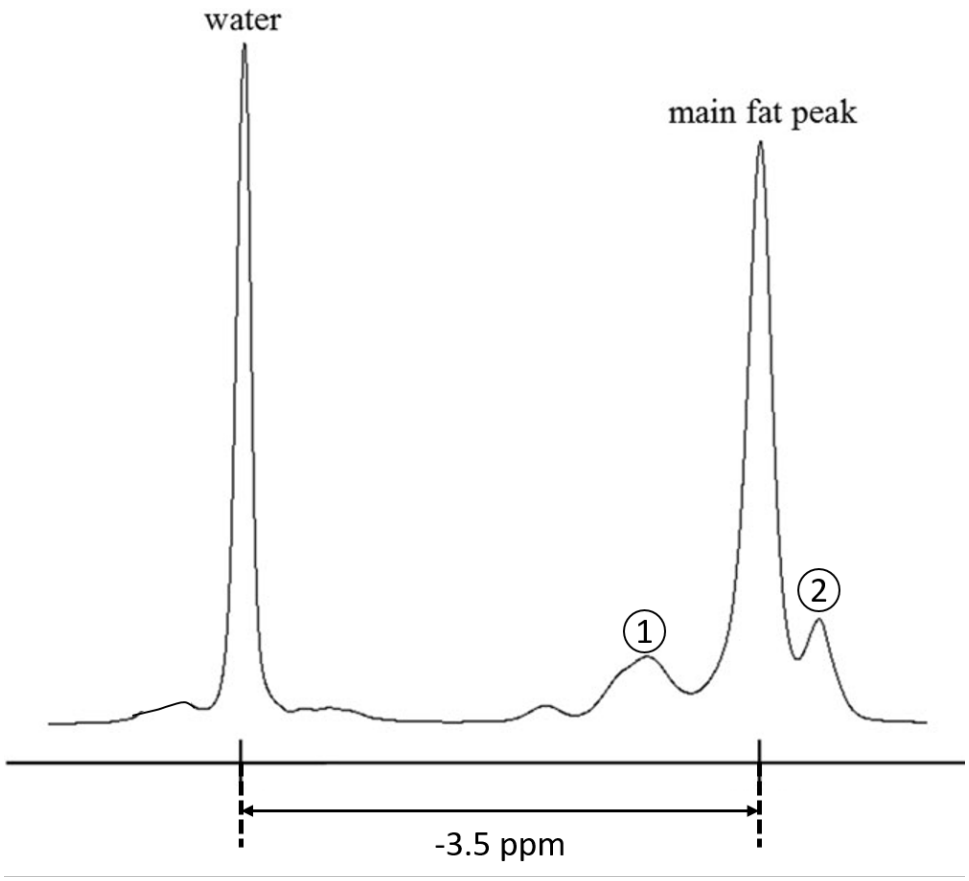

Figure 4.1 Illustration of spectral peaks for fat and water. The chemical shift difference between water peak and main fat peak is 3.5 ppm. It is important to note that fat actually has several additional peaks (1) and (2)).

For a simple gradient echo (GRE) sequence, the complex image as a function of time in the presence of water and fat will behave as [1, 2]:

$$\hat{\rho}(TE) = \hat{\rho}_w(TE) + \hat{\rho}_f(TE) \quad [4.2]$$

where $\hat{\rho}(TE)$ represents the complex image obtained at some chosen TE value, which contains unknown contributions from water and fat. The complex voxel signal in Eq. 4.2 can be rewritten as:

$$\hat{\rho}(TE) = \hat{\rho}_{w,m} + \hat{\rho}_{f,m} e^{-i\Delta\omega_{fw}TE} \quad [4.3]$$

The subscript m is used to denote the magnitude of the image and $\Delta\omega_{fw}$ represents the frequency difference between water and fat. The difference in phase generated by the frequency difference between water and fat as a function of TE is the key issue in this discussion.

Eq. 4.3 leads to a beat frequency pattern (see **Fig. 4.2**, for example) where the water and fat spins are in-phase (shown in **Fig. 4.3 (a)**) at a time when

$$\Delta\omega_{fw}TE_{in}(n) = 2n\pi \quad [4.4]$$

and out-of-phase (opposed phase) (shown in **Fig. 4.3 (c)**) at a time when

$$\Delta\omega_{fw}TE_{op}(n) = (2n+1)\pi \quad [4.5]$$

for later use, define 90° out-of-phase (shown in **Fig. 4.3 (b)**) as:

$$\Delta\omega_{fw}TE_{90}(n) = 2n\pi + \frac{\pi}{2} \quad [4.6]$$

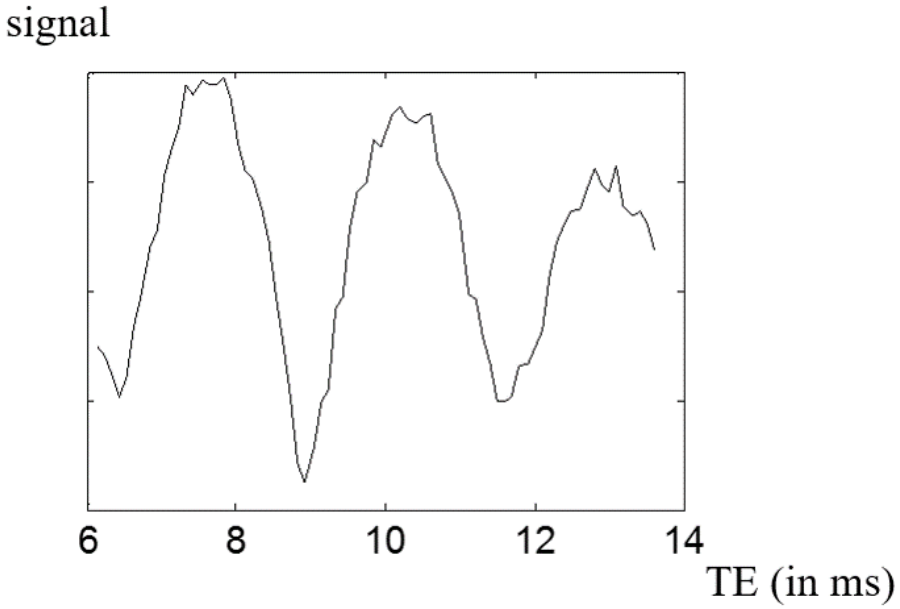

Figure 4.2 The beating envelope of the MR signal as a function of TE for one voxel containing both water and fat collected on a volunteer at 3T.

Fig. 4.3 shows that the spin behavior at three different phase angles for water and fat spins.

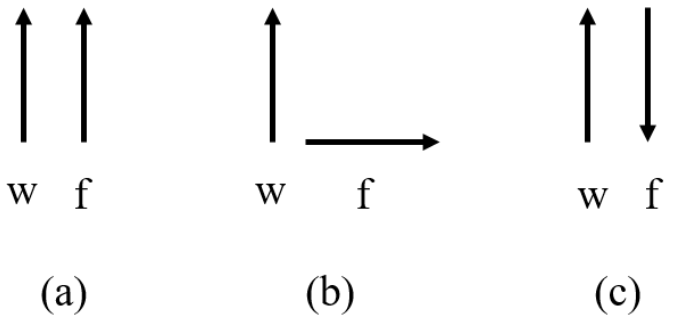

Figure 4.3 Phasor diagram representing water and fat spins when they are (a) in-phase, (b) 90° out-of-phase, and (c) 180° out-of-phase at $TE_{in}(n)$, $TE_{90}(n)$, and $TE_{op}(n)$, respectively.

When water and fat are 90° out-of-phase, assume there is a set of voxels containing only water or fat within each voxel as shown in **Fig. 4.4**. It is also assumed that the phase value of water at TE_{90} is $\phi_w(TE_{90}) = \frac{\pi}{4}\ rad$ and the phase value of fat at TE_{90} is $\phi_f(TE_{90}) = \frac{3\pi}{4}\ rad$. The plot of water and fat phase within each voxel is the 'dash-dot' line shown in **Fig. 4.4**.

As described in Chapter. 2, in practical situations, the phase signal collected from MR scanner has background field phase component, here, the background phase is assumed to smoothly increase from $0.2\ rad$ to $2.2\ rad$, which is the 'dot' line shown in **Fig. 4.4**. Hence, the true (net) phase value of each voxel is the sum of phase from water or fat signal and background field, which is the 'dash' line shown in **Fig. 4.4**. Note that the true phase of the three voxels containing fat exceed the range of $-\pi$ to π, thus, the collected phase would be wrapped, which is the 'solid' line shown in **Fig. 4.4**.

As discussed in Chapter 2, phase image is the only source of information used for QSM, thus, a clean and reliable original phase image is of great importance in QSM post processing to generate accurate susceptibility maps [2]. As previously described in this section, at water/fat out-of-phase time points, it is possible that the phase difference between water and fat combining with the background field phase will generate phase aliasing.

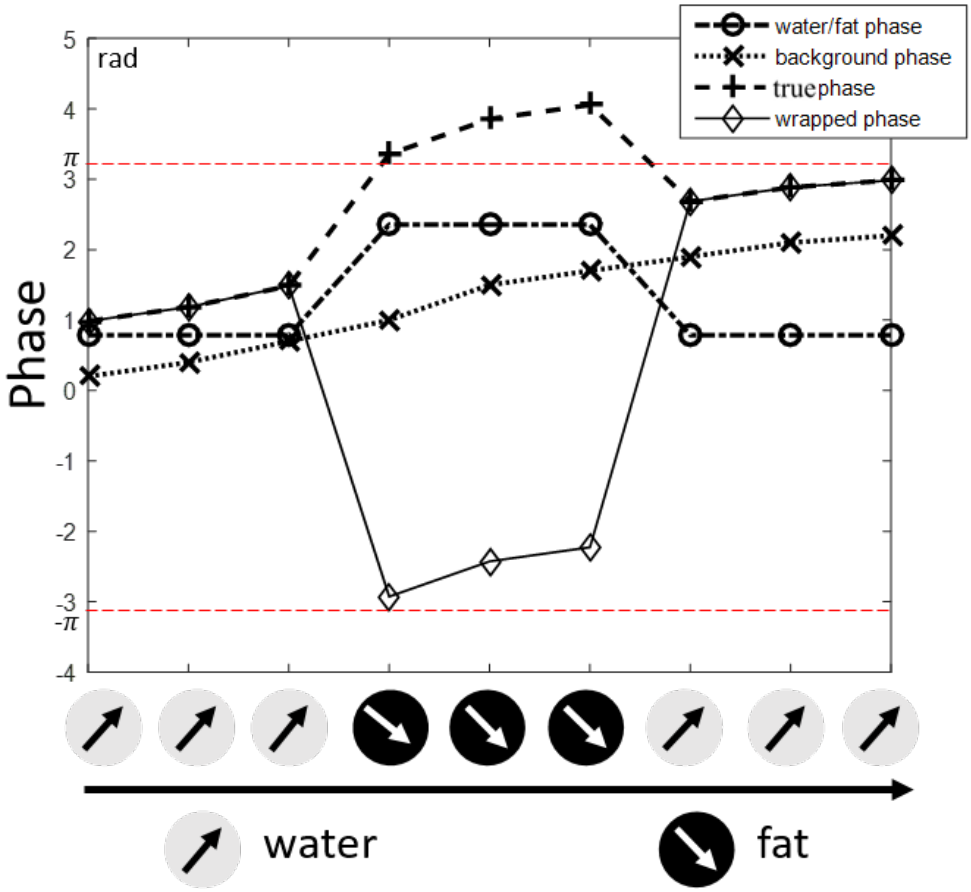

Figure 4.4 Illustration of a set of voxels containing either water or fat at 90° out-of-phase time point TE_{90} and plots of their phase values.

The region of interest, human neck has lots of fat presence and, furthermore, there is fat surrounding the carotid arteries. **Fig. 4.5** shows MR magnitude and phase images from a 3D SWI acquisition at water/fat in-phase and 90° out-of-phase echo times. As shown in **Fig. 4.5**, in human neck, there is fat presence around the carotid arteries and jugular veins, between the muscles and underneath the skin.

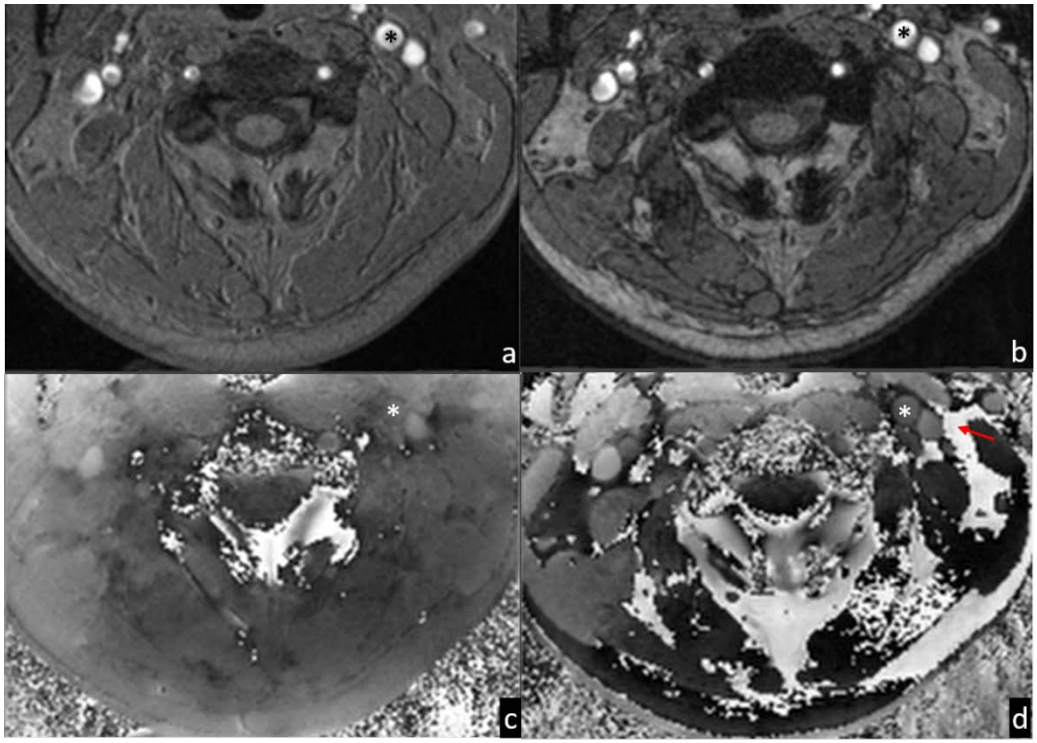

Figure 4.5 MR magnitude and phase images from a 3D SWI acquisition. (a) and (c) are magnitude and phase image from water/fat in-phase echo time ($TE = 5\ ms$). (b) and (d) are magnitude and phase image from water/fat 90° out-of-phase echo time ($TE = 11\ ms$). '*' indicates left carotid artery. The red arrow in (d) indicates phase aliasing due to water and fat chemical shift.

From the comparison between phase images from water/fat in-phase and out-of-phase echo times, it is shown that the phase behavior at water/fat out-of-phase echo time is more complicated than that at in-phase echo time. In order to generate accurate susceptibility

maps of carotid arteries, it is essential to collect data at water/fat in-phase echo times. Furthermore, as shown in **Fig 4.1**, the spectral peaks for fat and water, fat has more than one peak, which indicates that the fat stored in different parts of human body may have different chemical shift relative to water [1, 2]. Hence, careful experiments and measurements are needed to calculate the accurate water/fat in-phase and out-of-phase time.

4.2 Measurements of water/fat in-phase and out-of-phase time

In order to eliminate the phase variations induced by water/fat chemical shift, it is critical to find accurate water/fat in-phase times. Human thigh contains both muscle (which can be seen as water in MR imaging) and fat, and its physiological structure is relatively simple which makes it a good subject for studying the water/fat chemical shift.

Human leg experiment:

One MR dataset of human leg was collected on a 3T Verio system (Siemens, Erlangen, Germany) using a single-echo 2D SWI sequence. There were 76 acquisitions in total, imaging parameters are given in **Table 4.1**. Data were acquired in the transverse orientation.

Table 4.1 Imaging parameters for the human leg experiments (76 acquisitions) collected on one volunteer.

Acq. No.	1	2	3	…	76
$B_0\ (T)$	3	3	3	3	3
$TR\ (ms)$	16	16	16	16	16
$TE\ (ms)$	6.13	6.23	6.33	…	13.63
$FA\ (degrees)$	20	20	20	20	20
$BW\ (Hz/px)$	501	501	501	501	501
$Voxel\ Size\ (mm^3)$	2.68×2.68 ×3	2.68×2.68 ×3	2.68×2.68 ×3	2.68×2.68 ×3	2.68×2.68 ×3
$Matrix\ Size$	768×600 ×16	768×600 ×16	768×600 ×16	768×600 ×16	768×600 ×16

Figure 4.6 is an example of acquired magnitude and phase images at $TE = 6.13$. As shown by this data, it is easy to segment water and fat region on these images. Here, it is assumed that the water/fat in-phase times can be written as:

$$TE_{in}(n) = P * n + O \qquad [4.7]$$

where the slope P describes the periodicity due to their precession frequency difference $\Delta\omega_{fw}$, O is the offset value induced by time-independent phase offset, related to local conductivity and permittivity.

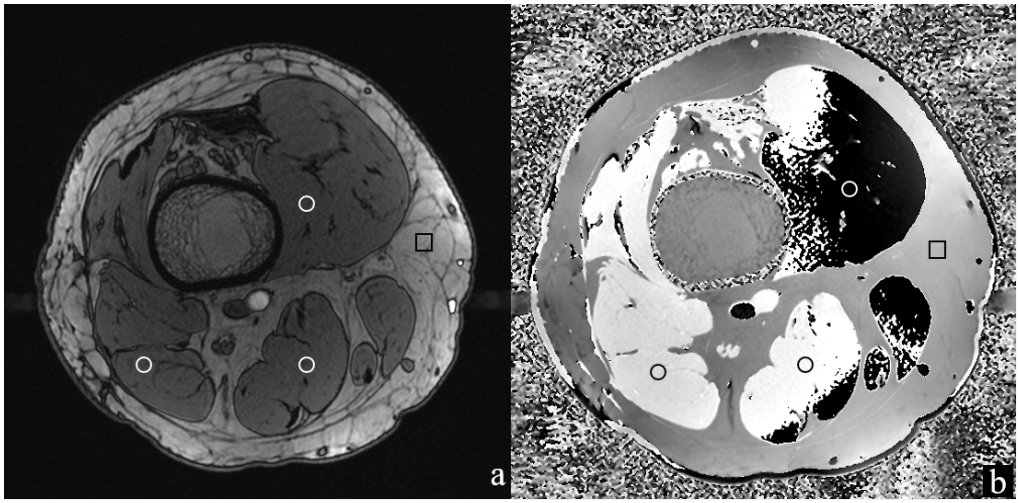

Figure 4.6 Magnitude image (a) and phase image (b) acquired at $TE = 6.13\ ms$. 'Circle' and 'square' indicates muscle (water) and fat area, respectively.

From Eqs. 4.1, the chemical shift between water and fat σ_{fw} leads to their precession frequency difference $\Delta\omega_{fw}$. Hence, $\Delta\omega_{fw}$ can be measured on frequency ($\not\Delta B$) maps generated from original phase images. And the phase offset can be measured on ϕ_0 maps.

The following steps were performed to generate the frequency ($\not\Delta B$) and ϕ_0 maps.

1) Anti-aliasing for original phase images

For a voxel contains water, the original phase evolution as a function of echo times is shown in **Figure 4.7 (a)**. There is phase aliasing on original phase images, so the first step was phase unwrapping. For this dataset, because the TE increment is $0.1\ ms$, the Catalytic Multiecho Phase Unwrapping Scheme (CAMPUS) concept was applied, which is starting with unwrapping the phase increment between first and second echo phase images, then

use them to unwrap the following echoes. The phase evolution of the same voxel on unwrapped phase images was shown in **Figure 4.7 (b)**.

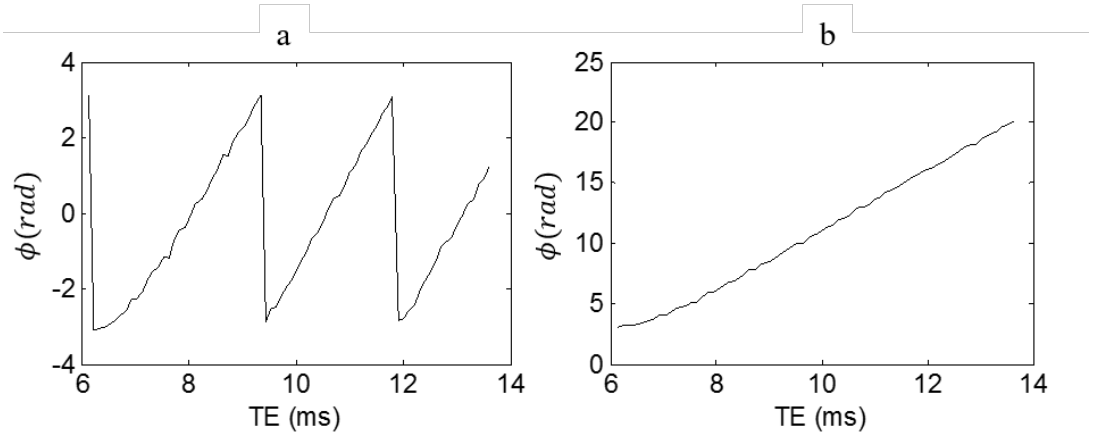

Figure 4.7 (a) Phase evolution of a voxel contains water on original phase images and **(b)** unwrapped phase images.

2) Generate frequency map using simple linear regression

A simple linear fitting was performed on the unwrapped phase images at all the echoes, a 2D quadratic fitting was applied to the results to remove the field variation induced by coil sensitivity. An example of generated frequency map is shown in **Figure 4.8 (a)**.

3) Generate ϕ_0 map

This dataset was collected on a left-handed system, Eqs. 2.15 can be rewritten as:

$$\phi_0(\vec{r}) = \phi(\vec{r}, TE) - \gamma \Delta B(\vec{r}) \cdot TE \qquad [4.8]$$

Hence, ϕ_0 map can be generated from unwrapped phase and $\gamma \Delta B$ map. An example of ϕ_0 map is shown in **Figure 4.8 (b)**.

4) Measurements of water/fat in-phase time

One area that contains only water and one area that contains only fat were chosen on both $\gamma\Delta B$ map and ϕ_0 map. The $\gamma\Delta B$ difference between water and fat was measured to be around $376\ Hz$, hence the slope P in Eqs. 4.7 was calculated to be around 2.66. The phase difference between water and fat on ϕ_0 map was measured to be around $0.71\ rad$, the offset O in Eqs. 4.7 was calculated to be around $-0.3\ ms$.

Hence, the water/fat in-phase time at 3T was found to be:

$$TE_{in}(n) = 2.66 * n - 0.3 \qquad [4.9]$$

where the unit of TE is millisecond and n is any positive integer which yields in-phase times of $2.36\ ms$, $5.02\ ms$, $7.68\ ms$, etc.

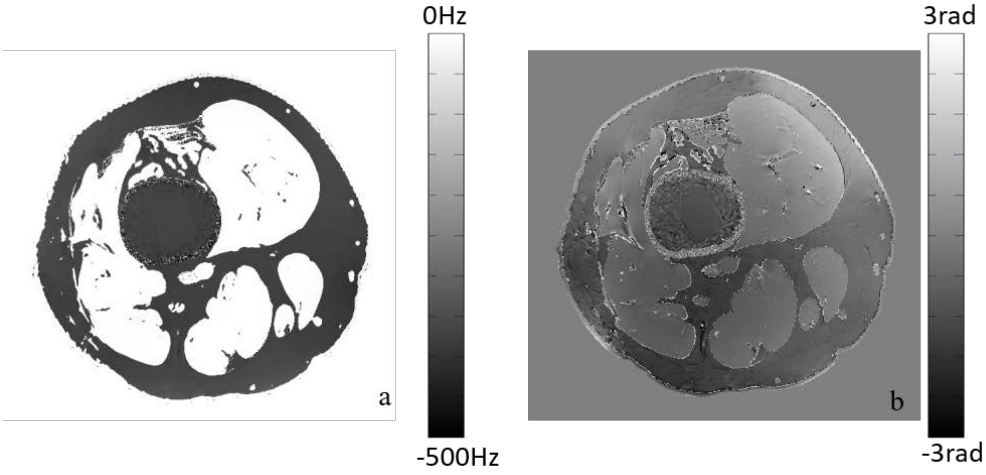

Figure 4. 8 (a) Frequency ($\gamma\Delta B$) map and **(b)** ϕ_0 map (the values were wrapped into the range of $-\pi$ to π.)

Human neck experiment:

After the human leg experiments, another dataset of human neck was collected on a 3T Verio system (Siemens, Erlangen, Germany) using a multi-echo 2D SWI sequence. There were 61 acquisitions collected on a volunteer in total, imaging parameters are given in **Table 4.2**. Data were acquired in the transverse orientation at 61 consecutive echo times (TE from 4.5 ms to 10.5 ms with 0.1 ms spacing).

Table 4.2 Imaging parameters for the human neck experiments (61 acquisitions) collected on one volunteer.

Acq. No.	1	2	3	…	61
$B_0\ (T)$	3	3	3	3	3
$TR\ (ms)$	90	90	90	90	90
$TE\ (ms)$	4.5	4.6	4.7	…	10.5
$FA\ (degrees)$	12	12	12	12	12
$BW\ (Hz/px)$	320	320	320	320	320
$Voxel\ Size\ (mm$	0.7×0.7 ×2.5	0.7×0.7 ×2.5	0.7×0.7 ×2.5	0.7×0.7 ×2.5	0.7×0.7 ×2.5
$Matrix\ Size$	256×256 ×6	256×256 ×6	256×256 ×6	256×256 ×6	256×256 ×6

The following steps were performed to calculate the water/fat in-phase echo times for this dataset.

1) Anti-aliasing for original phase images

Since the TE increment between two echoes was 0.1 ms, CAMPUS concept was applied. Starting with unwrapping the phase from $TE = 5\,ms$ (which should be around the water/fat in-phase time according to the results from the leg experiment) using transitional phase unwrapping method, the quality guided 3D phase unwrapping algorithm (3DSRNCP). Then use the resulting unwrapped phase to unwrap neighboring echoes.

2) ϕ_0 estimation

From Eq. 2.15, ϕ_0 is a time-independent term that is related to local conductivity and permittivity, thus, ϕ_0 term is associated with the starting point of water/fat in-phase times. Here, A linear fitting was performed on the unwrapped phase images from all the echoes to generate ϕ_0 maps. **Figure 4.9** shows a result of generated ϕ_0 maps.

3) Measurements of the water/fat in-phase echo time

Two areas (surrounding the jugular veins) that contain only water and only fat were chosen on unwrapped phase images. The phase of water and fat were represented by the mean values of each area. The evolution for the phase of water and fat and their phase difference over TE were plotted, as shown in **Figure 4.10**. In order to calculate the water/fat in-phase echo time, a polynomial fitting was performed to the phase of water and fat, respectively ($R^2 > 0.99$) to generate two smooth trend lines, as shown in **Figure 4.11**. Note that, the

phase difference between water and fat equals to zero indicates water/fat in-phase. For the fat surrounding the carotid arteries and jugular veins, the in-phase times at 3T were found to be:

$$TE_{in}(n) = 2.5 * n + 0.1 \quad [4.10]$$

where the unit of TE is millisecond and n is any positive integer which yields in-phase times of $2.6\ ms, 5.1\ ms, 7.6\ ms$, etc.

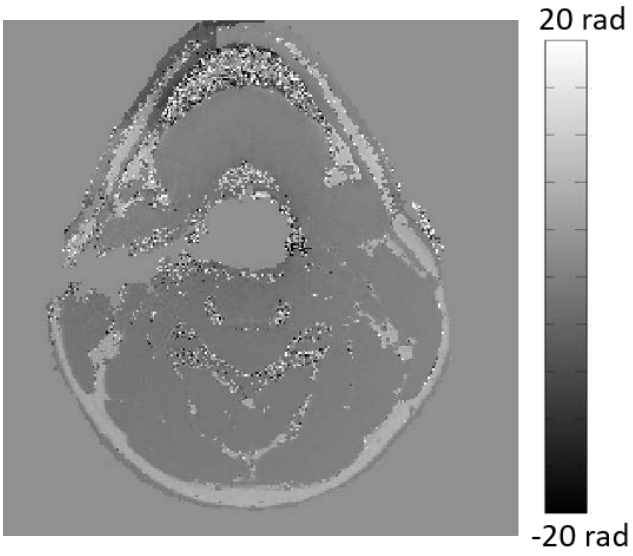

Figure 4.9 ϕ_0 map generated by a linear fitting of the unwrapped phase images from all echoes.

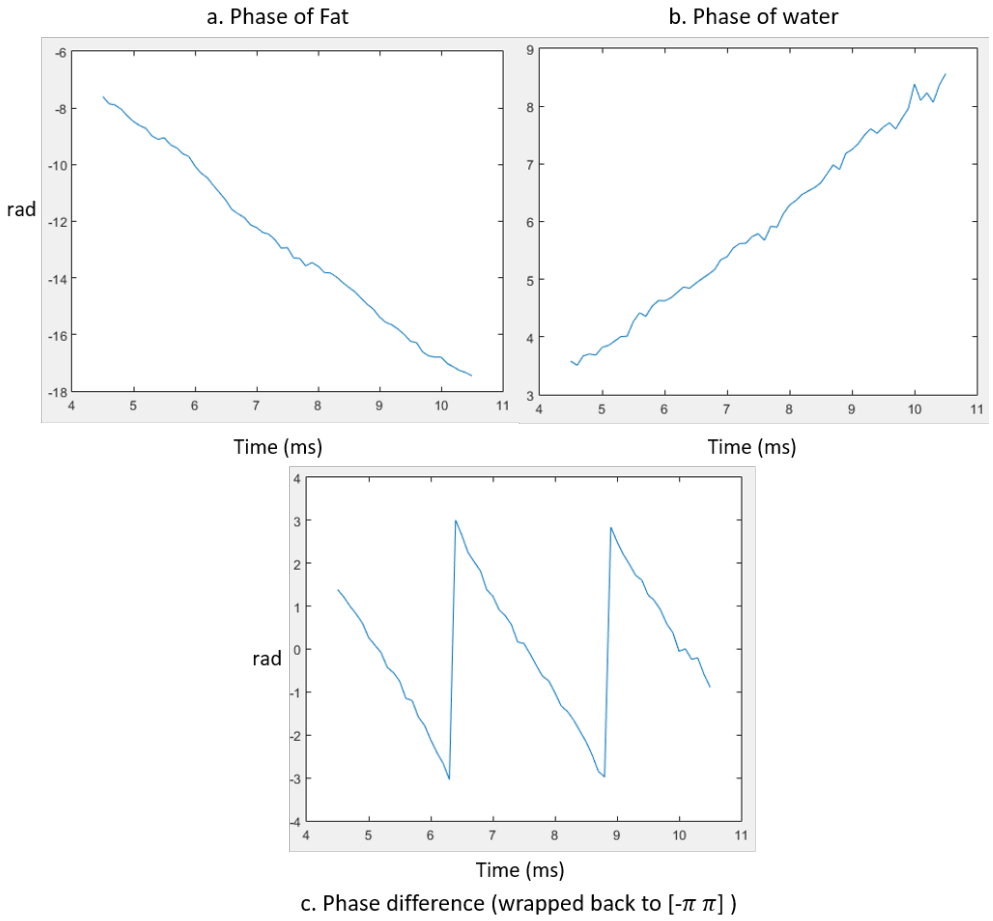

Figure 4.10 (a) The evolution for the phase of fat and their phase difference over TE. **(b)** The evolution for the phase of water over TE. (c) The evolution for the phase difference between water and fat over TE (wrapped back to $[-\pi\ \pi]$).

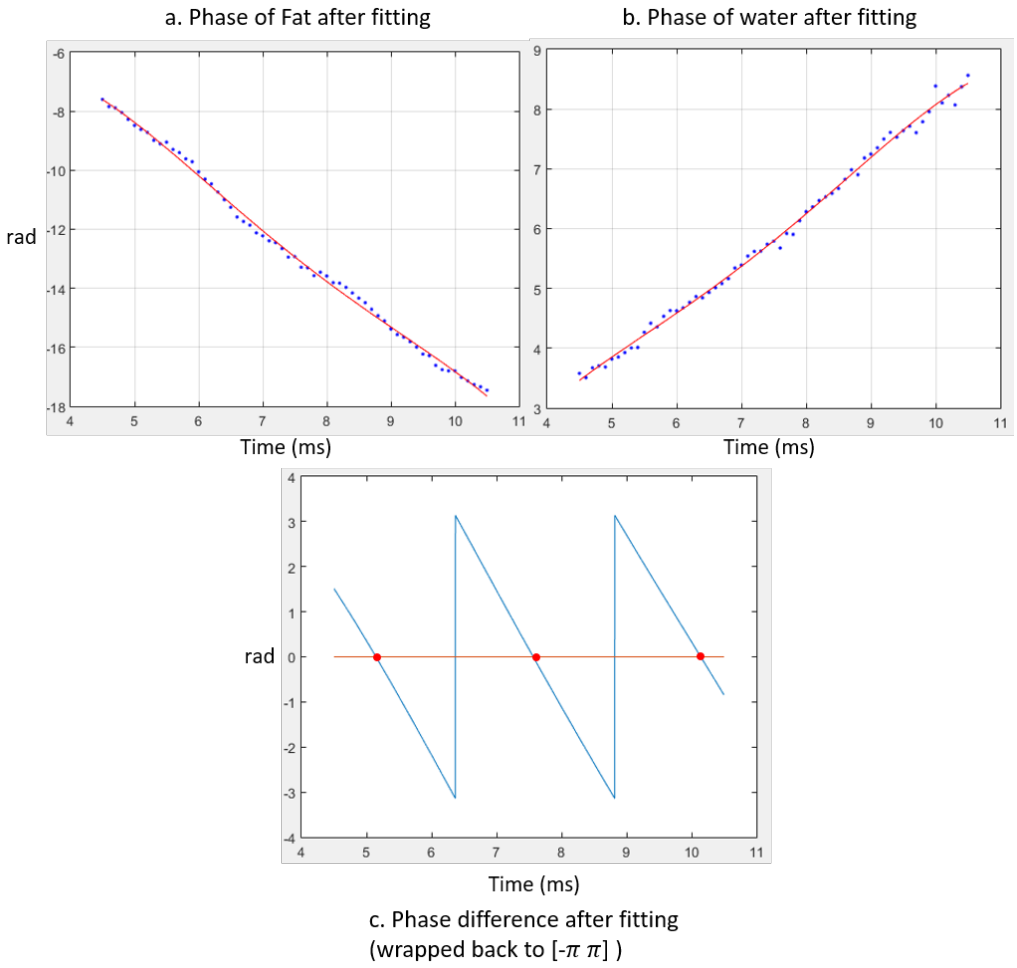

Figure 4.11 (a) The trend line generated form a polynomial fitting of the evolution for the phase of fat and their phase difference over TE. **(b)** The trend line generated form a polynomial fitting of the evolution for the phase of water over TE. **(c)** The evolution for the phase difference between water and fat calculated using two trend lines over TE (wrapped back to $[-\pi\ \pi]$). Red dots on **(c)** represents water/fat in-phase time points.

4.3 Proposed method for QSM of carotid atherosclerosis

As discussed in Chapter 3, the primary goal of clinical carotid vessel wall and plaque imaging is to identify vulnerable plaque, which has high likelihood of developing ischemic stroke in the brain. The major types of atherosclerotic plaque are classified as lipid core, intraplaque hemorrhage (IPH) or thrombosis, and calcification, etc [3]. These plaque components provide a nice susceptibility contrast, with lipid core and calcification being diamagnetic, hemorrhage or thrombosis that contains iron being paramagnetic. As can be seen from Eqs. 2.23, the susceptibility difference between a blood vessel and surrounding tissue are related to the oxygen saturation. For arterial blood, the normal oxygen saturation Y of a healthy individual varies from 94% to 100%, hence the susceptibility of arterial blood can be approximated as $0\ ppm$ [2]. Thus, the susceptibility difference between arterial blood, vessel wall and different plaque types (lipid core, hemorrhage, and calcium) makes QSM a promising tool for characterizing atherosclerotic plaque and identifying its vulnerable features.

Although QSM technique has the potential for carotid plaque imaging, no existing study has successfully implemented QSM in neck. The reason is that the application of QSM in the neck is complicated by challenges that are not likely to present in brain QSM. These additional challenges include: (i) the presence of air (esophagus) closing to the carotid arteries, this will cause phase aliasing on original phase images due to the unwanted global

phase induced by these interfaces and hence, introduce artifacts during background field removal processing step, (ii) the presence of fat, as discussed in Section 4.2, the water/fat chemical shift effect will cause discontinuities in phase behavior at all but in-phase echo times, and (iii) the potential presence of plaque with high susceptibility (hemorrhage or calcification) that will cause phase aliasing inaisde the plaque region which is the region of interest. This problem is demonstrated in **Figure 4.12**. As discussed in Chapter 2, the concentional spatial domain phase unwrapping approaches may fail here, thus, temporal domain phase unwrapping methods are needed.

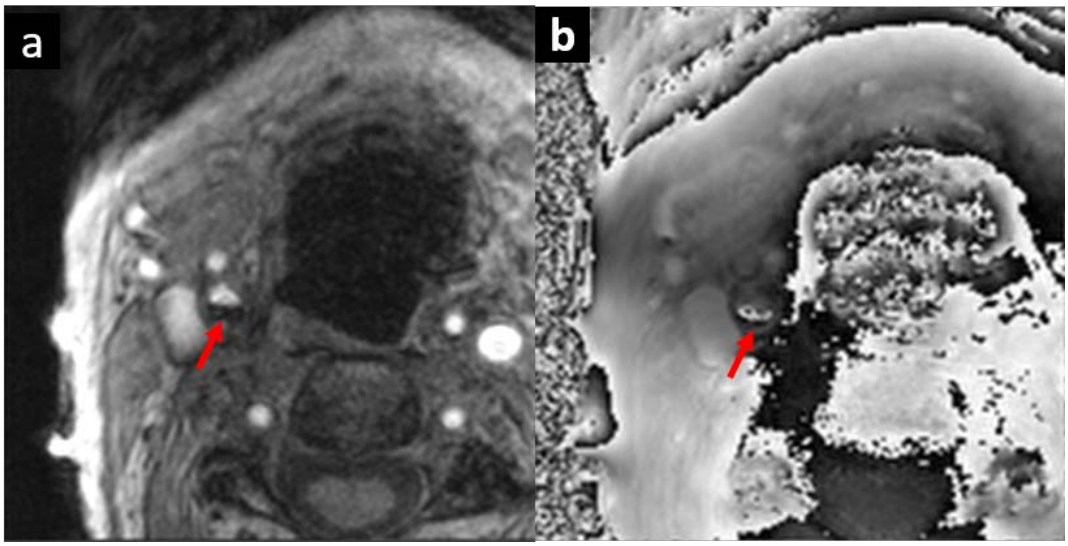

Figure 4.12 Demonstration of phase aliasing caused by the high susceptibility of plaque. Magnitude image (a) and original phase image (b) from $TE = 7.5\ ms$. Red arrow is showing the plaque and the aliasing on phase image.

In order to overcome the challenges described above, we proposed a technique for neck QSM by developing both optimized data acquisition method and image reconstruction method that is able to successfully implement QSM techniques for carotid plaque imaging.

(i) Proposed method for data acquisition

When designing a SWI acquisition, the first thing that needs attention is the choice of echo times. As discussed in Section 4.2, in order to eliminate phase aliasing caused by water/fat chemical shift effect, echo times need to be at water/fat in-phase time points. Eqs. 4.10 can be used to calculate the water/fat in-phase echo times in neck at 3T, which yields 2.6 ms, 5.1 ms, 7.6ms, etc.

Also, considering that calcified plaque, hemorrhage or thrombosis may have high susceptibility, it can cause rapid dephasing of the signal and phase aliasing at long echo times. Hence, short echo times are needed for SWI acquisition in the neck. However, as discussed in Chapter 2 Section 2.2, SWI sequence requires flow compensation and the nulling gradients limit the shortest available echo time. 5.1 ms was tested to be the shortest water/fat in-phase echo time this sequence can achieve. Table 4.3 shows the proposed protocol for carotid SWI acquisition. Echo time of 5.1 ms may not be short enough to avoid the phase aliasing due to high susceptibility of the plaque. Hence, we proposed to (1) generate equivalent $TE = 0.63\ ms$ phase images by complex dividing the phase images from $TE = 5.1\ ms$ echo and $TE = 4.47\ ms$ echo (or $TE = 5.73\ ms$), this equivalent $TE = 0.63\ ms$ phase does not have any phase aliasing even with the presence of a plaque that has very high susceptibility, thus, this equivalent $TE = 0.63\ ms$ phase can be used to

unwrap phase images from longer in-phase echoes ($TE = 5.1\ ms$ and $TE = 7.6\ ms$), and susceptibility maps can be generate from unwrapped phase images from longer echoes ($TE = 5.1\ ms$ or $TE = 7.6\ ms$). (2) by collecting $TE = 4.47\ ms$ ($270°$ out-of-phase), $TE = 5.1\ ms$ (in-phase), and $TE = 5.73\ ms$ ($90°$ out-of-phase) echoes, we will have enough information to perform water/fat separation and quantification.

Table 4.3 Imaging parameters for proposed protocol for carotid atherosclerosis imaging.

Acq. No.	1	2	3	4
$B_0\ (T)$	3	3	3	3
$TR\ (ms)$	15	15	15	15
$TE\ (ms)$	4.47	5.1	5.73	7.6
$FA\ (degrees)$	12	12	12	12
$BW\ (Hz/px)$	300	300	300	300
$Voxel\ Size\ (mm^3)$	0.6×0.6×2	0.6×0.6×2	0.6×0.6×2	0.6×0.6×2
$Matrix\ Size$	256×256 ×64	256×256 ×64	256×256 ×64	256×256 ×64
$Flow\ Comp.$	Yes	Yes	Yes	Yes

(ii) Proposed method for image post-processing

1) water/fat separation

From Eq. 4.3, for a homogeneous field, the complex signal of a voxel can be written as:

$$\hat{\rho}(TE) = \hat{\rho}_{w,m} + \hat{\rho}_{f,m} e^{-i\Delta\omega_{fw}TE} \quad [4.11]$$

The subscript m is used to denote the magnitude of the image, thus $\hat{\rho}_{w,m}$ represents the magnitude of water signal and $\hat{\rho}_{f,m}$ represents the magnitude of fat signal.

When $\Delta\omega_{fw}TE_{90} = \frac{\pi}{2} + 2n\pi$, the complex signal can be rewritten as:

$$\hat{\rho}(TE_{90}) = \hat{\rho}_{w,m} - i\hat{\rho}_{f,m} \quad [4.12]$$

when $\Delta\omega_{fw}TE_{in} = 2n\pi$, the complex signal can be rewritten as:

$$\hat{\rho}(TE_{in}) = \hat{\rho}_{w,m} + \hat{\rho}_{f,m} \quad [4.13]$$

when $\Delta\omega_{fw}TE_{270} = \frac{3\pi}{2} + 2n\pi$, the complex signal can be rewritten as:

$$\hat{\rho}(TE_{270}) = \hat{\rho}_{w,m} + i\hat{\rho}_{f,m} \quad [4.14]$$

Hence, a simple algorithm could be used to obtain water and fat images:

$$\hat{\rho}_{w,m} = \frac{1}{2}(\hat{\rho}(TE_{90}) + \hat{\rho}(TE_{270})) \quad [4.15]$$

$$\hat{\rho}_{f,m} = \hat{\rho}(TE_{in}) - \hat{\rho}_{w,m} \quad [4.16]$$

However, in practice, the static field is not perfectly homogeneous, considering the presence of $\phi_{\Delta B}$ and ϕ_0, Eq. 4.11 can be rewritten as:

$$\hat{\rho}(TE) = (\hat{\rho}_{w,m} + \hat{\rho}_{f,m}e^{-i\Delta\omega_{fw}TE})e^{-i\gamma\Delta BTE}e^{-i\phi_0} \quad [4.17]$$

where $\phi_{\Delta B} = \gamma\Delta BTE$ is the phase gained due to the presence of field inhomogeneities and ϕ_0 is a time independent global phase offset. Acquiring three datasets from one in-phase scan, one 90° out-of-phase scan, and one 270° out-of-phase scan makes it possible to find $\phi_{\Delta B}$ and ϕ_0, then correct phase images for $\phi_{\Delta B}$ and ϕ_0.

$\gamma\Delta B$ and ϕ_0 maps are obtained via from a simple linear fitting using phase images from all three echoes.

The next step is to correct the complex image for $\phi_{\Delta B}$ and ϕ_0 effect by multiplying $\hat{\rho}(TE)$ by $e^{i\gamma\Delta BTE+i\phi_0}$, hence, the complex image after correction can be written as:

$$\hat{\rho}'(TE_{in}) = \hat{\rho}(TE_{in})e^{i\gamma\Delta BTE+i\phi_0} \quad [4.18]$$

$$\hat{\rho}'(TE_{90}) = \hat{\rho}(TE_{90})e^{i\gamma\Delta BTE+i\phi_0} \quad [4.19]$$

$$\hat{\rho}'(TE_{270}) = \hat{\rho}(TE_{270})e^{i\gamma\Delta BTE+i\phi_0} \quad [4.20]$$

Finally, water and fat images can be generated using Eq. 4.15 and 4.16.

2) Phase unwrapping using CAMPUS approach

From Eqs. 2.15, for a right-handed system, the phase at voxel location $\vec{r}$ at time TE_i using a single echo SWI sequence can be written as [4]:

$$\phi(\vec{r}, TE_i) = -\gamma\Delta B(\vec{r})TE_i + \phi_0 + \phi_M + \theta_{l(i)}(x) + \eta(\vec{r}) \quad [4.21]$$

where x is the coordinate of the voxel along the readout direction, $\gamma\Delta B(\vec{r})$ is the local field variation, ϕ_M is the flow-induced phase, $\theta_{l(i)}(x)$ is the eddy-current induced phase along the readout direction, variable $l(i)$ depends on the direction (positive or negative) of the readout gradients. And $\eta(\vec{r})$ represents the noise-induced phase variation. It is assumed that the eddy-current behavior reaches a steady state such that all the positive (or negative) gradients induce the same linear phase [4].

For our proposed protocol, three echoes are collected at TE of 4.47 ms, 5.1 ms, and 5.73 ms ($\Delta TE = 0.63ms$) with full flow compensation using three single echo SWI acquisitions. Hence, it is assumed that the eddy-current induced phase $\theta_{l(i)}(x)$ is the same for all three echoes and flow-induced phase ϕ_M is fully compensated.

The following steps are performed to unwrap the phase images from our proposed protocol. Note that the term h(r) is ignored in the following derivations.

(1) Interecho phase increments were computed with complex division of adjacent echo images. Note that because these phase images are from three scans with the same direction of readout gradient, the eddy-current induced phase will be canceled after the complex division. The phase increments from the first echo to the second echo and from the second echo to the third echo can be written as:

$$\Delta\phi_{21}(\vec{r}, \Delta TE) = -\gamma \Delta B(\vec{r}) \Delta TE \quad [4.22]$$

$$\Delta\phi_{32}(\vec{r}, \Delta TE) = -\gamma \Delta B(\vec{r}) \Delta TE \quad [4.23]$$

(2) $\gamma \Delta B(\vec{r})$ can be obtained with a Simple addition of the adjacent phase increments:

$$\Delta\phi_{3,1}(\vec{r}, 2\Delta TE) = 2\gamma \Delta B(\vec{r}) \Delta TE \quad [4.24]$$

thus,

$$\gamma \Delta B(\vec{r})_{estimated} = \frac{\Delta\phi_{3,1}(\vec{r}, 2\Delta TE)}{2\Delta TE} \quad [4.25]$$

(3) Using Eq. 4. 25 in Eqs. 4. 22 and 4.23, the phase increments between the first three echoes can be unwrapped to give $\Delta\phi_{21}^{un}$ and $\Delta\phi_{32}^{un}$. The phase image for the first echo can be unwrapped using the estimated local field variations and the echoshift term. But first, the eddy-current induced phase $\theta(x)$ needs to be removed from the measured phased images. Here, a simple linear fitting is performed to estimate eddy-current induced phase

and after the removal of this component, the measured phase at the first echo can be written as:

$$\phi(\vec{r},\ TE_1) = -\gamma \Delta B(\vec{r}) TE_1 + \phi_0 - 2\pi N(\vec{r}) \quad [4.\ 26]$$

where the integer $N(\vec{r})$ is the number of phase wraps at $\vec{r}$. To unwrap $\phi(\vec{r},\ TE_1)$, we will need to estimate ϕ_0, which is assumed to be almost constant over the whole image. We can also assume that $\phi_0 \in [-\pi, \pi)$. Hence, $N(\vec{r})$ can be estimated as:

$$\frac{-\phi(\vec{r}, TE_1) - \gamma \Delta B(\vec{r}) TE_1}{2\pi} - \frac{1}{2} \leq N(\vec{r}) < \frac{-\phi(\vec{r}, TE_1) - \gamma \Delta B(\vec{r}) TE_1}{2\pi} + \frac{1}{2} \quad [4.27]$$

Once $N(\vec{r})$ is estimated, ϕ_0 can be calculated with Eq. 4.26. With both $N(\vec{r})$ and ϕ_0 estimated, the phase at first echo can be unwrapped using Eq. 4.26.

(4) Finally, combining the unwrapped first echo with the subsequent unwrapped phase increments, all remaining echoes can be unwrapped. **Figure 4. 13** shows the original phase images and unwrapped phase images at all echoes.

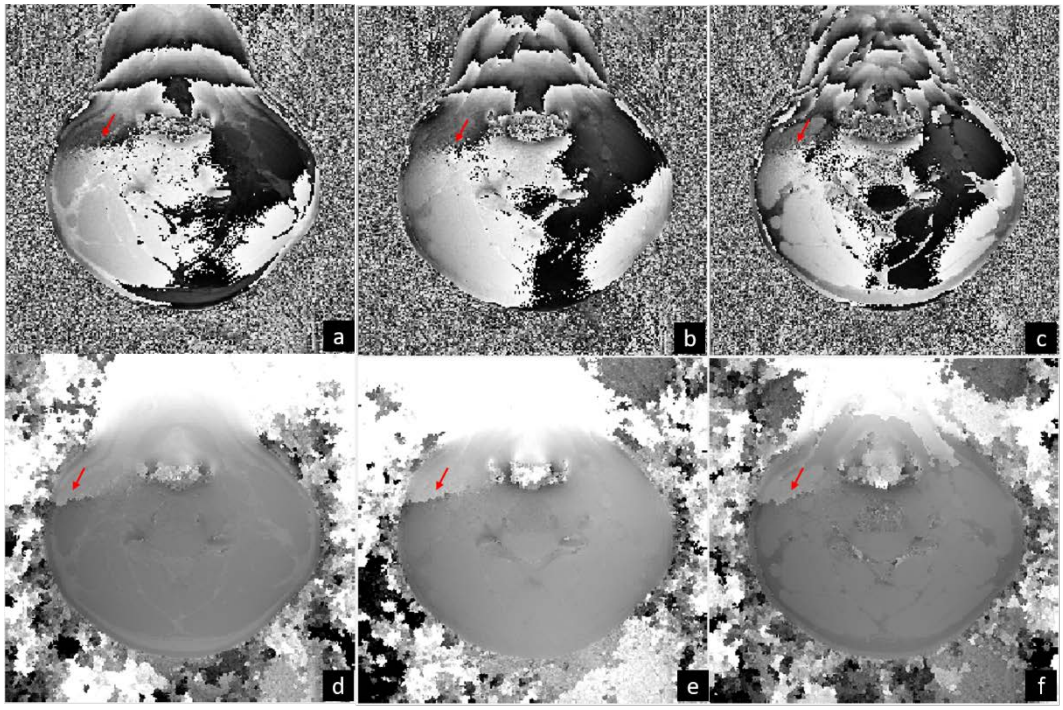

Figure 4.13 Original phase images of $TE = 4.47\ ms$ **(a)** and $TE = 5.1\ ms$ **(b)**, and $TE = 5.74\ ms$ **(c**) collected on the same healthy volunteer with a 3D SWI sequence. Unwrapped phase images of $TE = 4.47\ ms$ **(d)** and $TE = 5.1\ ms$ **(e)**, and $TE = 5.74\ ms$ **(f)**. Note that unwrapped phase images still have phase abnormalities (red arrows) which is caused by cusp artifacts.

3) Background field removal using SHARP

As mentioned previously, the air in esophagus has very high susceptibility, thus rapid T2* dephasing effect causing signal loss even at shorter TEs. The bones (teeth and spine) also have very high susceptibility. Thus these regions also suffer from phase aliasing or even zero signal. These regions will exacerbate the artifacts during the background field removal

and the inverse process. Thus, all the noisy regions need to be removed before applying SHARP [5]. A mask was generated manually from first echo magnitude images with unity for regions around the carotid arteries with high signal intensities, and zero for other regions. This mask was then applied to unwrapped phase images, where the phase data was manually examined for any remnant noisy pixels and update the mask to remove them. This resultant mask was used for SHARP processing to remove background field.

4) Generate susceptibility maps

An inverse filter was applied to the resulting phase images to generate susceptibility maps. **Figure 4.14** shows the filter phase image after applying SHARP and generated susceptibility maps.

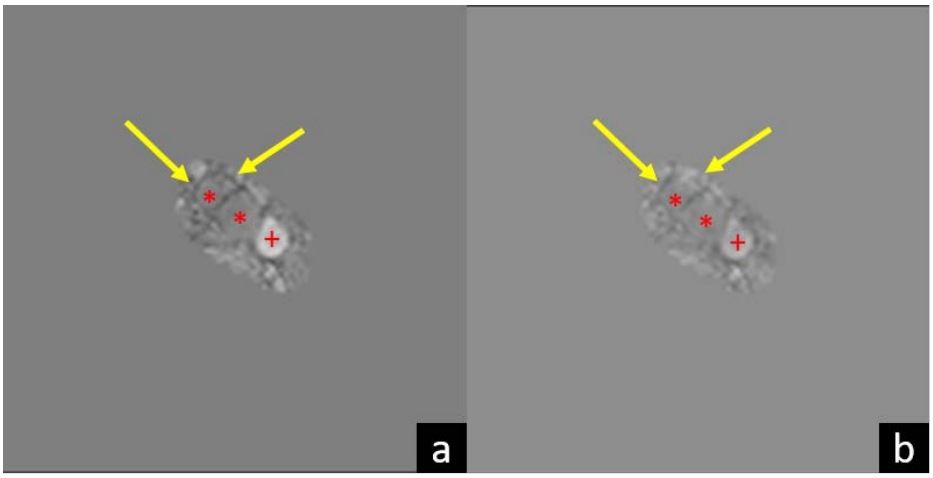

Figure 4.14 (a) Filtered phase after applying SHARP. **(b)** Susceptibility map. * indicates carotid arteries and + indicates jugular vein. The yellow arrows show the diamagnetic vessel wall.

4.4 Results from QSM of carotid atherosclerosis

Figure 4.15 shows the QSM results from a patient with potential IPH in the carotid arteries. This patient was imaged on a 3T scanner (Verio, Siemens Healthcare, Erlangen, Germany) using a three-echo 3D SWI sequence. The imaging parameters were TE1 = 5.18 msec, TE2 = 7.67 msec, and TE3=10.09 msec, FA = 15°, BW = 485 Hz/pixel, voxel size = 0.5 x 0.5 x 2 mm^3 and matrix size = 336 x 448 x 64. The susceptibility maps were reconstructed using the phase images from TE=7.76 msec echo.

Figure 4.16 shows the QSM results from a patient with potential calcification in the carotid arteries. This patient was imaged on a 3T scanner (Verio, Siemens Healthcare, Erlangen, Germany) using a three-echo 3D SWI sequence. The imaging parameters were TE1 = 5 msec, TE2 = 7 msec, and TE3=10 msec, FA = 20°, BW = 488 Hz/pixel, voxel size = 0.5 x 0.5 x 2 mm^3 and matrix size = 320 x 320 x 40. The susceptibility maps were reconstructed using the phase images from TE=7 msec echo.

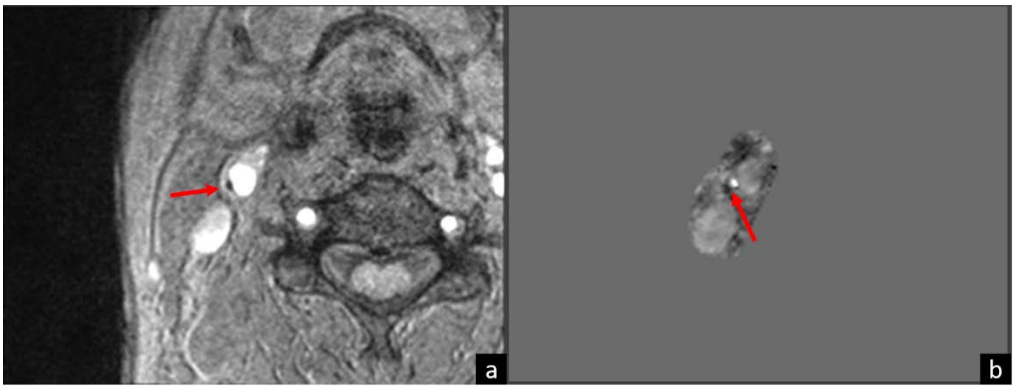

Figure 4.15 (a) Magnitude showing thickened wall (the dark region pointed by the arrow) and **(b)** this region is showing paramagnetic susceptibility on QSM which indicates that this plaque is laden with iron (potential thrombosis).

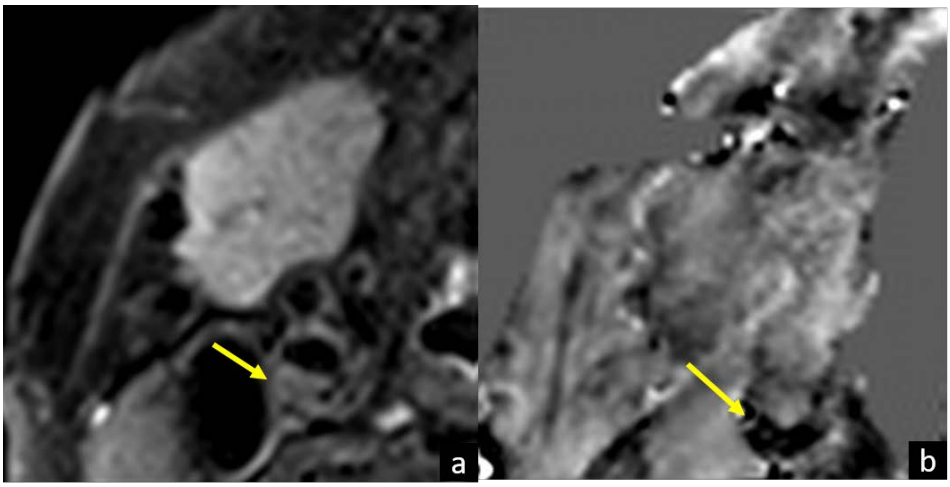

Figure 4.16 (a) Black-blood image **(b)** susceptibility map. Black-blood image shows thicken wall (yellow arrow), on QSM, this region is showing dark (diamagnetic) indication calcification.

References

1. Haacke EM, Brown RW, Thompson MR, Venkatesan R. Magnetic Resonance Imaging: Physical Principles and Sequence Design. 1st ed. Wiley-Liss; 1999.

2. Haacke EM, Reichenbach JR, editors. Susceptibility Weighted Imaging in MRI: Basic Concepts and Clinical Applications. 1st ed. Wiley-Blackwell; 2011.

3. Underhill, Hunter R., et al. "MRI of carotid atherosclerosis: clinical implications and future directions." Nature Reviews Cardiology 7.3 (2010): 165-173.

4. Feng W, Neelavalli J, Haacke EM. Catalytic multiecho phase unwrapping scheme (CAMPUS) in multiecho gradient echo imaging: removing phase wraps on a voxel-by-voxel basis. Magn Reson Med 2013;70(1):117–26.

5. Schweser F, Deistung A, Lehr BW, Reichenbach JR. Quantitative imaging of intrinsic magnetic tissue properties using MRI signal phase: an approach to in vivo brain iron metabolism? NeuroImage 2011;54(4):2789–807.

Chapter 5. Conclusions and Future Directions

In this thesis, the importance of MR carotid atherosclerosis imaging and the advantages and limitations of current MR magnitude-base approaches were discussed. The most important part of MR carotid atherosclerosis imaging is to identify the vulnerable plaque, in other words, to detect hemorrhage (IPH) and calcification inside a plaque [1]. QSM was considered to be promising due to its superb sensitivity to the susceptibility contrast induced by iron (hemorrhage) and calcium (calcification). However, existing QSM techniques have not been successfully implemented in the neck due to several challenges.

In Chapter 4, we proposed a new protocol for neck QSM including both data acquisition strategy and post-processing methods to overcome the complicated phase behavior in the neck and generate reliable susceptibility maps. This proposed method for carotid atherosclerosis imaging includes two parts: firstly, collecting 3D SWI data at the water-fat in-phase TEs. Without any water-fat out-of-phase effects, the phase information from these echoes will be used for QSM reconstructions. Secondly, collecting one dataset at the water-fat 90° out-of-phase echo time and one at the water-fat 270° out-of-phase echo time. These out-of-phase datasets and in-phase datasets were used to perform water/fat separation and quantification. Combining two parts together enables the visualization of calcium, iron

inside the plaque as well as fat fraction of the neck. Our results have shown that the proposed protocol enabled both QSM of the carotid arteries and water/fat separation in the neck. And QSM results, as expected, were able to detect different types of plaque in carotid arteries and, therefore, recognize vulnerable features. In clinical settings, susceptibility maps can provide information on the components of the plaque while magnitude-based techniques (such as the multi-contrast approach with T1, T2, PD -weighted imaging) [2] can be used to obtain morphology information, such as the location of plaque, the size of the stenosis, and the status of fibrous cap. Thus, combining QSM with other magnitude-based techniques is promising to improve the diagnosis of carotid atherosclerosis which should lead to a more robust and easy to use approach clinically.

Considering the gold-standard in carotid atherosclerosis imaging is *ex vivo* histological analysis of the plaque. Thus, further work in patients comparing QSM results with *ex vivo* histological analysis is necessary to determine the accuracy of this method.

References

1. Underhill, Hunter R., et al. "MRI of carotid atherosclerosis: clinical implications and future directions." Nature Reviews Cardiology 7.3 (2010): 165-173.

2. Yuan, Chun, et al. "MRI of carotid atherosclerosis." Journal of nuclear cardiology 15.2 (2008): 266-275.